INSTITUTE OF PLASMA PHYSICS

NAGOYA UNIVERSITY

Energy and Momentum Deposition to Plasmas due to the Lower Hybrid Wave by a Finite Source

Noriyoshi Nakajima, Hirotada Abe* and Ryohei Itatani+

(Received - Sept. 27, 1981)

IPPJ-546 Oct. 1981

RESEARCH REPORT

NAGOYA, JAPAN

Energy and Momentum Deposition to Plasmas due to the Lower Hybrid Wave by a Finite Source

Noriyoshi Nakajima, Hirotada Abe* and Rychei Itatani+

(Received - Sept. 27, 1981)

IPPJ-546 Oct. 1981

Futher communication about this report is to be sent to the Research Information Center, Institute of Plasma Physics, Nagoya University, Nogoya 464, Japan

*Present Address: Department of Electronics, Kyoto University, Kyoto 606, Japan

ENERGY AND MOMENTUM DEPOSITION TO PLASMAS DUE TO THE LOWER HYBRID WAVE BY A FINITE SOURCE

Noriyoshi Nakajima*, Hirotada Abe, and Ryohei Itatani
Department of Electronics, Kyoto University, Kyoto 606, Japan

ABSTRACT Heating and current generation due to the lower hybrid wave are studied using the particle simulation. In contrast with previous work, where only the single mode is treated, main interests of this work are focused on the physical problems on a propagation cone consisting of many Fourier-expanded modes. It is found that the trajectory of the propagation cone is well described up to the lower hybrid resonance layer using both cold plasma approximation and the WKB method. An ion cross-field drift due to the ponderomotive force is observed. It is a main discovery that the modes in the higher side of the spectrum of the antenna play a key role for creation of the ion high energy tail. This process cannot be explained by the linear theory and is called the cascade process judging from the time variation of the damping of each mode. The particle model is significantly improved using the elongated grid and the quadric spatial interpolation. Many applications of this model to the simulations on other problems are expected to be very fruitful in the research of the plasma physics and nuclear fusion.

* present address : Institute of Plasma Physics, Nagoya University, Nagoya 464, Japan

1. INTRODUCTION

Wave motions can be used as carriers for energy and momentum. Actually, the wave can be excited on the plasma surface and transmitted to the central core of the plasma, where its energy and momentum can be absorbed by the ions and electrons. In this way, heating and/or current generation can be attained.

The lower hybrid (LH) wave has been a candidate to be adopted for the auxiliary heating or current generation in tokamaks. Its generator may be technically feasible even at the present time. It has been a very important subject to investigate its availability for these purposes physically. Therefore, a number of experimental [1-5], theoretical [6-12], and computational [13-19] works have been performed until now.

Experimentally, the ion heating has been already confirmed [3,4] and the possibility of the current generation has been also suggested [5]. On the other hand, some incomprehensible results have been shown in these experiments. The theoretical studies on the LH wave carried out by many authors successfully explain a part of phenomena in the experiments, however, it is too complex to solve all the problems through the purely theoretical approach, because the linear and nonlinear phenomena influence on each other in the nonuniform system.

In these problems, the self-consistent computer simulation is useful. Because the wave-particle interactions are essential in the case of the LH wave, the particle model is preferred.

On the basis of these consideration, Abe et al. studied the most fundamental case, that is, wave propagations, heating, and

current generation on a single mode with the LH frequency [13,15]. From these simulation results, it has been suggested that the wave produces the ion high energy tail near the lower hybrid resonance (LHR) layer and wave energy is mainly deposited on its tail [15]. As indicated by Karney [9], the energy of the tail can be moved to the bulk through the ion-ion collision and, therefore, the temperature of the bulk ion can be increased. Furthermore, the current produced at the plasma surface can be explained by the trapping of the electron due to the electrostatic potential of the single mode[13].

In the case of tokamak experiments, generally, a finite antenna, which we call the grill antenna [7], is used. In contrast with a single mode exciter used in the simulation studies [13,15], this kind of antenna excites localized waves whose spectrum is broad. These localized waves include many physical problems which are concerned with the propagation cone [12], ponderomotive force due to the strong localized field [20], linear and/or nonlinear multimode wave-particle interactions and so on. From this point of view, Decyk et al. [16-18] and Matsuda et al. [19] performed simulations using finite length antenna modelled. Each of them obtains many results, while one may encounter a trouble when one wants to connect some simulation results with the physical mechanisms about tokamak experimental results, that is to say, their system sizes in the periodic direction are so small that two propagation cones excited by a bi-directional antenna interfere each other due to the periodic condition and are strongly disturbed. In addition, broadness of the wave number spectra of the antennas over the lower $k_{\parallel m}$ modes is not enough due to the

smallness of the system sizes in the periodic direction.

To solve this problem fundamentally, it is inevitable to improve the particle simulation model itself, because the number of the spatial grids is limited due to performance of today's computers. One of such improvements is directed to the usage of the elongated grid [21] and/or the higher order spatial interpolations [22-24]. In the case of the LH wave, the following points should be considered: The parallel wave length is much longer than the perpendicular one and then the grid spacing parallel to the external magnetic field can be lengthened compared with the perpendicular one to the degree that the shortest wave length in the system is about 6 grid spacings. In this case, usually, the grid spacing becomes so longer than the Debye length that the numerical instability grows [25] and/or the total energy conservation becomes worse. As a trial to improve this, the use of the quadric spatial interpolation is proposed by Lewis et al. originally. This method is called method 2/2 [22]. They concluded, however, that the significant improvements were not obtained from the results of two or three tests unfortunately [22,23].

On the other hand, Abe et al. [24] compared between the modified method 2/2 using the quadric interpolation together with the Fast Fourier Transform method and the usual models using the linear interpolation. They estimated the influence of the numerical error due to use of the finite spacing of the spatial grids and the finite time step on the total energy conservation by observing the magnitude of its fluctuation. As a result, they obtained a scaling law which indicated the dependence of the fluctuation of the total energy upon both the simulation parameters

and a parameter η which showed a measure of the goodness of the model. Furthermore, they found out from η the heating time τ_H defined as the time during which the total energy increased by 25 % and showed that τ_H was proportional to $1/\eta^2$ [26]. From many tests, they concluded that in comparison of τ_H with each other the quadric interpolation was better by about 20 times than the linear interpolation. We think, therefore, that it is hopeful to adopt this modified method 2/2.

In Sec. 2, we summarize the theories concerning the propagation cone in the nonuniform plasma, the stochastic accelerations of the particle, and the current generation. In Sec. 3, we have explained the improvement of the simulation model and the antenna modelled by considering the properties of the LH wave discussed in Sec. 2. In Sec. 4, we present the simulation results and some analyses of them concerning the wave propagations, ion heating, the high energy tail formation of ions, the effects of the ponderomotive force on plasma, the electron heating and current generation, and the electron velocity distribution. In Sec. 5, a summarization of this work, relations of it with other works, and the remained problems will be presented.

2. THEORETICAL CONSIDERATIONS

2.1. The propagation of the localized LH wave [12]

The propagation of the LH waves in an inhomogeneous plasma can be approximated using the WKB method. Assuming that an electrostatic approximation is valid and that a plasma is cold, we may

obtain,

$$\frac{\partial}{\partial x}(K_{xx}\frac{\partial}{\partial x}E_z)=-K_{zz}\frac{\partial^2}{\partial z^2}E_z \quad , \tag{1}$$

where

$$K_{xx}=1-\frac{\omega_{pe}^2}{\omega^2-\Omega_e^2}-\frac{\omega_{pi}^2}{\omega^2-\Omega_i^2} \quad , \tag{2}$$

$$K_{zz}=1-\frac{\omega_{pe}^2}{\omega^2}-\frac{\omega_{pi}^2}{\omega^2} \quad . \tag{3}$$

When the pump frequency is between Ω_i and Ω_e, where Ω_i and Ω_e are the ion and electron cyclotron frequencies, respectively, Eq. (1) may be solved using the Fourier analysis with respect to the Z direction and the WKB method [12],

$$E_z(x,k_z)=E_z(x_0,k_z)A(x,x_0)\exp[i|k_z|g(x)] \quad , \tag{4}$$

where

$$g(x)=\int_{x_0}^{x}\{-\frac{K_{zz}(x')}{K_{xx}(x')}\}^{\frac{1}{2}}dx' \quad , \tag{5}$$

$$A(x,x_0)=\{\frac{K_{xx}(x_0)K_{zz}(x_0)}{K_{xx}(x)K_{zz}(x)}\}^{\frac{1}{4}} \quad , \tag{6}$$

and $E_z(x_0, k_z)$ is a value at $x=x_0$.
Furthermore, Eq. (4) is inversely Fourier-analyzed to be

$$E_z(x,z)=\frac{A(x,x_0)}{2\pi i}\int_{-\infty}^{\infty}dz'E_z(x_0,z')$$
$$\{P\ \frac{1}{z-z'-g(x)}-P\ \frac{1}{z-z'+g(x)}$$
$$+i\pi\delta[z-z'-g(x)]+i\pi\delta[z-z'+g(x)]\} \quad . \tag{7}$$

Equation (7) shows that the wave trajectory may be described by the characteristic curves of Eq. (1)

$$z=\pm g(x)+c. \tag{8}$$

If $E_z(x_0, z)$ is localized along z, then its propagation cones are formed along the characteristic curves given by Eq. (8). It is evident from Eq. (1) that the propagation cones in a homogeneous plasma are written by lines:

$$z=\pm(-K_{zz}/K_{xx})^{1/2}x+c. \tag{9}$$

From Eq. (9) it is found that when the cone travels x_s in the x direction, it travels a distance of about $(m_i/m_e)^{1/2}x_s$ in the z direction. The wave amplitude of each Fourier mode is estimated by Eq. (6). The function $A(x, x_0)$ is nearly equal to unity before the LHR layer and increases just before it. The WKB method is valid only when $(dk_x/dx)/k_x<<k_x$, and, therefore, it is invalid in the neighborhood of the LHR layer. Taking account of thermal effects allows us to treat both cold electron plasma wave and hot ion plasma wave which is converted from the former at near the LHR layer. In this case, singular fields in Eq. (7) alter to non-singular fields [27].

2.2. Two types of stochastic acceleration [8,9,14]

Two types of stochastic acceleration mechanism exist for electrostatic monochromatic waves with ion cyclotron harmonics. They are called the resonant and nonresonant stochastic accelerations [14].

The following three conditions must be satisfied in order that the significant resonant stochastic acceleration may occur for ions with Maxwellian velocity distribution.

(i) $\omega/\Omega_i \lesssim 10$. (10)

(ii) For the parallel resonant velocity

$$v_{\parallel mr} = \frac{\omega - n\Omega_i}{k_{\parallel m}} ,$$

where n is an integer nearest to ω/Ω_i,

$$|v_{\parallel mr}|/v_{Ti0} < 3 \sim 4 , \quad (11)$$

(iii) For the normalized wave amplitude

$$a = (\omega/\Omega_i)^{-2/3} \alpha = (\omega/\Omega_i)^{-2/3} (k_{\perp m}/\Omega_i)^2 e\phi_m/m_i ,$$

$$a \gtrsim 1/5 . \quad (12)$$

For nonresonant stochastic acceleration to occur, the following two conditions are required.

(iv) $$v_\perp > \frac{\omega}{k_{\perp m}} , \quad (13)$$

(v) $a \gtrsim 1/4$. (14)

Concerning the auxiliary heating of a usual tokamak plasma by the LH waves, the nonresonant stochastic acceleration is dominant because $\omega/\Omega_i \sim 20 \sim 40$. In the case of simulations, however, we have used reduced mass which leads to a pump frequency $\omega \sim 3 \sim 8\,\Omega_i$, and, therefore, there is a possibility of the observation of the resonant stochastic acceleration. In order to avoid the occurrence of the resonant stochastic acceleration, therefore, the con-

dition (ii) is used when the simulation parameters are chosen.

2.3. Quasilinear diffusion and steady-state velocity distribution of electron [10,11]

Using the quasilinear diffusion and the collisional terms, the evolution of the electron distribution function f on the parallel velocity is expressed by [11]

$$\frac{\partial f}{\partial \tau} = \frac{\partial}{\partial w} D(w) \frac{\partial f}{\partial w} + \frac{3}{2} \frac{\partial}{\partial w} \{ \frac{1}{C(w)} (\frac{1}{w} \frac{\partial f}{\partial w} + f) \} \quad , \tag{15}$$

where $\tau = \nu_c t$, $w = v_{\parallel e} / v_{Te0}$, $D(w) = D_{RF} (v_{\parallel e}) / (v_{Te0}^2 \nu_c)$, and D_{RF} is a quasilinear diffusion coefficient due to the RF, ν_c is a collision frequency. Usually, C(w) is different between real plasmas and simulation plasmas. In the case of the former, $C(w) = w^2$, while in the case of the latter, C(w) is a complex function of w [28]. In any case, the solution to Eq. (15) in the steady state, i.e. $\partial f / \partial \tau = 0$, is given by

$$\ln f = - \int \frac{w}{1 + \frac{2}{3} w C(w) D(w)} \, dw \quad . \tag{16}$$

Fisch [10] shows analytically that when

$$D(w) = D \qquad \text{for } w_1 < w < w_2 \quad ,$$

$$= 0 \qquad \text{otherwise} \quad , \tag{17}$$

f has a plateau in the region of $w_1 < w < w_2$ on the condition of $w_1 D >> w_2 - w_1 >> 1/w_1$. From these results, he advocates the method of generation of the steady current by the LH wave in tokamak plasmas

[10,11].

In this work, we will neglect details of dependence of C(w) on w in the simulation plasmas and set $C(w)=w^2$ the same as in the real plasmas. As shown later (Sec. 4.), we could not obtain the completely steady-state distribution of the electron in the simulation run from the reason of insufficient performance of the used computer. Therefore, we think that it is insignificant to improve the accuracy of C(w) for the simulation plasmas in this work.

Because the periodic boundary condition is adopted in the parallel direction in the present simulation model, the wave spectrum becomes discrete and the diffusion coefficient D(w) is given as [29]

$$D(w)=\sum_m \frac{\pi\omega\,(e\phi_m/T_e)^2}{2\nu_c w_{ph\|m}}\,\delta(w-w_{ph\|m}) \quad , \tag{18}$$

where $w_{ph\|m}=v_{ph\|m}/v_{Te0}$. Including the effect of the particle trapping by the large-amplitude waves, we extend this as follows [29];

$$D(w)=\sum_m D_m(w)=\sum_m \frac{\pi\omega\,(e\phi_m/T_e)^2}{2\nu_c w_{ph\|m} w_{trm}} \quad \text{for } -\frac{w_{trm}}{2}<w-w_{ph\|m}<\frac{w_{trm}}{2} \quad ,$$

$$= 0 \qquad \text{otherwise} \quad , \tag{19}$$

where $w_{trm}=v_{trm}/v_{Te0}=4(e\phi_m/T_{e0})^{1/2}$. When the neighboring trapping regions are overlapped, larger value of D_m is chosen.

3. SIMULATION MODEL

For advanced works, as mentioned in Sec. 1, it is necessary to solve the problem concerning how to treat large physical systems within the limits of today's computer performance. To do so, it is inevitable to consider physical natures of the LH wave and physical and numerical natures of the simulation model.

As mentioned in Sec. 2, the LH wave travels about $(m_i/m_e)^{1/2}x_s$ in the z direction which is parallel to the external magnetic field when it travels x_s in the x direction. When we use the simple cloud-in-cell model [30] with square grid, therefore, the grid number in the x direction is required to be about $(m_i/m_e)^{1/2}$ times as large as that in the z direction. In order to decrease the grid number in the z direction, we can use elongated grids whose distance in the parallel direction is about $(m_i/m_e)^{1/2}$ times as long as that in the perpendicular direction. On the basis of the arguments in Sec. 1, we should use the quadric interpolation [24] as a spatial interpolation for z to decrease the numerical error. The linear spatial interpolation used in the cloud-in-cell model has a better spatial resolution and is adopted for that with respect to x.

The phased wave guide array, so called grill antenna, is used as an antenna through which the wave is injected into a plasma. We model the grill antenna by modifying Eq. (9) in Ref. [13] as

$$\rho_s=\rho_{s0}\delta(x-x_s)f(z,t) \quad . \tag{20}$$

In this work, we use the four-phased wave guide array, that is,

$$f(z,t) = \sin(\omega_0 t - n\delta) \quad \text{for } n\frac{L_A}{4} < z < (n+1)\frac{L_A}{4} \quad ,$$

$$(n=0,\ 1,\ 2,\ \text{and } 3)$$

$$= 0 \qquad \text{for } L_A < z < L_z \quad , \tag{21}$$

where L_A is the length of the antenna, L_z is the length of the system in the z direction, and δ is the phase difference between the neighboring segments of the wave guide. Equation (21) is Fourier-expanded as

$$f(z,x) = \sum_{m=-\infty}^{\infty} A_m(\delta,R) \sin\left[\frac{2\pi m}{L_z}\left(z - \frac{L_z}{2R}\right) - \left(\omega_0 t - \frac{3}{2}\delta + \pi\right)\right] \quad , \tag{22}$$

where $$A_m(\delta,R) = \frac{1}{R} \frac{\sin\left(\frac{m\pi}{4R}\right)}{\frac{m\pi}{4R}} \cos\left(\frac{m\pi}{4R} - \frac{\delta}{2}\right) \cos\left(\frac{m\pi}{2R} - \delta\right) \quad ,$$

$$R = L_z / L_A \quad . \tag{23}$$

This antenna emits traveling waves with both the positive and negative phase velocities to the z direction. The phase difference δ is optimized according to the purpose. When $\delta = \pi$, the spectrum is symmetric, and when $\delta = \pi/2$, the spectrum is asymmetric with the larger components in the positive z direction as shown in Fig. 1. In this work, $\delta = \pi/2$ is adopted, furthermore, the components traveling to the negative z direction are let be vanished in order to save the system size. Generally, a grill antenna emits two propagation cones traveling reversely each other, however, each cone separates as the wave propagates into the high density

region. Therefore, the natures of the separated cones are investigated by the antenna which excites a single cone.

Following two points are altered compared with the previous work [13].

Initial plasma density increases exponentially with x away from the antenna. Initial electron temperature profile can be changed such that it increases exponentially with x. Computationally, this can be realized: the temperature is discretized into the 12 levels corresponding to the 12 regions with same area into which the system is divided along x and in each of which the increase of the kinetic energy is calculated (see Sec. 4.2.).

Reflection condition of particles from two limiters is altered as follows; the particles reaching the left limiter are reflected into the system with random velocities whose standard deviation is the initial surface temperature and those reaching the right limiter are reflected into the system such that no machroscopic current is generated [31].

4. SIMULATION RESULTS

Two runs we call Run 1 and Run 2 were performed. Main simulation parameters are presented in Tab. 1. A mass ratio 100 is used. The parameters for Run 1 are set such that the injected RF power deposits mainly on ions. Normalized parallel resonant velocity $v_{\parallel mr}/v_{Ti0}$ for each Fourier mode presented in Tab. 2 is set in order to avoid the resonant stochastic acceleration, explained in Sec. 2. Initial electron and ion temperatures for Run 1 are uniform in space. Normalized phase velocity $v_{ph\parallel m}/v_{Te0}$ for

each Fourier mode presented in Tab. 3 is chosen so as to avoid the electron Landau damping.

In the case of Run 2, normalized phase velocity v_{phm}/v_{Te0} for each Fourier mode is chosen smaller than that in Run 1 such that the injected RF power deposits mainly on electrons through the electron Landau damping. In this case, the spatial variation of the initial electron temperature is essential and it is set increasing exponentially to be $T_{e0R=12}/T_{e0R=1}=4.2$ where $T_{e0R=j}$ is the initial electron temperature in the region j (see Sec. 3). The initial ion temperature is uniform in space, and $T_{i0}=T_{e0min}$.

In the case of the LH wave experiments aiming at current generation, the LHR layer has sometimes been out of the system so as to avoid forming surface current. When the LHR layer is not in the system, the LH wave penetrates a plasma and reflects on the wall. In this case, observed phenomena are too complex to discuss. In this simulation, therefore, we set the LHR layer being in the system, because we prefer investigation of physics of current generation to its optimization.

In order to get the surface current and heating due to nonlinear effects little, furthermore, the RF power is decreased somewhat compared with that for Run 1. It is too high, however, to avoid the surface current and heating completely.

4.1. Wave propagation for Run 1

Figure 2 shows the contour of $\phi_c(x,z,t)$, where $\phi_c(x,z,t)$ is an interferogram between the observed potential and the source signal (see Eq. (12) in Ref. [13]) and its correlation time was

chosen to be $4T$ ($T=2\pi/\omega_0$). In this figure, distance to the z direction is scaled down to one sixteenth compared with that to the x direction. We can see that the LH wave forms a propagation cone and penetrates deeply into a plasma continuously. After the LH wave reaches the neighborhood of the LHR layer ($t\gtrsim 12T$), the propagation cone has not changed so much. As shown by a bold curve in the Fig. 2(b), the propagation cone is well approximated by Eq. (8).

In order to investigate the thermal and nonlinear effects of a plasma on the wave propagation in detail, we calculated the x-dependent Fourier modes of $\phi_c(x,z,t)$ for z, i.e., $\phi_{cm}(x,t)$, which are shown in Fig. 3. By plotting the phase of $\phi_{cm}(x,t)$, we calculated $k_{\perp mr}(x)$ which are real parts of complex perpendicular wave number $k_{\perp m}=k_{\perp mr}+ik_{\perp mi}$ and compared them with theoretical values derived from the linear dispersion relation [13,32], as shown in Fig. 4.

As shown in Tab. 3, the wave for m=3 corresponding to $\phi_{c3}(x,t)$ has a parallel phase velocity of $v_{ph\parallel m}/v_{Te0}=13.7$ and a perpendicular wave number of $(k_{\perp mr}v_{Ti0}/\Omega_i)^2\sim 0.6$ near the turning point, T_p, where the turning point [6] is defined as a point at which a hot branch and a cold branch cross each other and after which the wave is evanescent. The numerical results shown in Fig. 4 indicate no wave damping, that is, $k_{\perp mi}=0$ up to T_p. At $t=12T$, the observed wave for m=3 little damps and its calculated $k_{\perp mr}(x)$ well agrees with the theoretical value, as shown in Figs. 3(a) and 4(a). After that time, it increases in its amplitude around T_p corresponding to Eq. (6). At $t=20T$, its maximum attains to 1.7 times larger than that at $t=12T$. Therefore, a mode conversion [6]

from a cold mode (a cold electron plasma wave) to a hot mode (a hot ion plasma wave) is expected to occur.

In fact, a reflection wave was observed after the wave reached the LHR layer at $t \gtrsim 12T$. This reflected wave can be identified as follows. For a unidirectionally-traveling wave, the phase $\theta(x)$ of ϕ_{cm} defined as $\int k_{\perp mr}(x')dx' + \delta_m$ must be a smooth curve likely as that in the case of m=5, while for the wave a with reflected one the phase $\theta(x)$ is disturbed as those in the cases of m=3 and m=4, as shown in Fig. 5. We performed a calculation in order to identify whether this reflected wave is the cold mode of the same branch for the incident wave or the hot mode shown in Fig. 4. We assumed the interferograms of the injected wave and reflected wave as

$$\phi_{cm}^{(i)} = A\sin(k_{\parallel m}z + \int_{x_0}^{x} K_{\perp mr}^{(i)}dx + \delta_m^{(i)}) \quad , \tag{24}$$

$$\phi_{cm}^{(r)} = AR\sin(k_{\parallel m}z + \int_{x_0}^{x} k_{\perp mr}^{(r)}dx + \delta_m^{(r)}) \quad , \tag{25}$$

where the superscript (i) and (r) denote the incident and reflected waves, respectively. The hot or cold $k_{\perp ir}$ obtained from the linear dispersion relation was substituted to the $k_{\perp mr}^{(r)}$ for $\phi_{cm}^{(r)}$. Adjusting the phases $\delta_m^{(i)}$, $\delta_m^{(r)}$, and the reflective index R, we tried to make a fit such that the curve of phase $\theta(x)$ derived from Eqs. (24) and (25) resembled that of m=3 in Fig. 5. As a result, it is considered that the reflective wave is the cold mode and the reflective index R is about 0.15. This phenomenon will be discussed again in Sec. 5.

In contrast with the wave for m=3, the wave for m=9 is subject to the nearly uniform damping, as shown in Fig. 4(c), while the linear dispersion relation predicts no damping, i.e. $k_{\perp mi}=0$, up to T_p, as shown in Fig. 3(c). Furthermore, the wave is considered to penetrate deeply into the evanescent region beyond T_p. Figure 3(c) shows that the observed $k_{\perp mr}$ deviates from the theoretical $k_{\perp mr}$ in the neighborhood of T_p. Decyk et al. also observed this penetration [18]. However, it contrasts to our observation in the point that their observed $k_{\perp mr}$ well agreed with the theoretical $k_{\perp mr}$ even in the evanescent region.

Time variation of the wave damping for $\phi_{cm}(x,t)$, which were calculated between 4T and 40T, was examined in detail. It is a conclusion that the wave for higher m which means the slower perpendicular phase velocity is damped faster. In the case of the lower m, for example, the wave for m=3 with a large phase velocity always shows an overshoot near T_p, while this phenomenon is not clear at t=12T but is clear after this time. Because these phenomena may be closely connected with the formation of the ion high energy tail, they will be discussed in Sec. 4.2.

Figure 6 shows the wave spectra of a potential, $\phi_m(x,\omega)$, which are Fourier-analyzed with respect to both z and t. The growth of side band waves was observed with respect to lower m. The frequencies of the prominent side band waves are higher than the pump frequency. In the case of m=3, for example, the main side band frequency ω_s is slightly larger than a frequency $(\omega_{LH})_{max}=(\Omega_e\Omega_i)^{1/2}=10\Omega_i$, that is, $\omega_s=1.6\omega_0=10.1\Omega_i$. For identification of this mode, we calculated the linear dispersion relation and searched a normal mode with $\omega=\omega_s$. As a result, the wave

is concluded to be a cold LH wave which satisfies $\omega=\omega_{LH}(1+(m_i/m_e)(k_{\parallel m}/k_m)^2)^{1/2}$ and has a large perpendicular wave length $\lambda_\perp=2\pi/k_{\perp mr}\gtrsim L_x$. Furthermore, the phase $\theta(x)$ of the wave was observed to have a jump by about π at $x\sim 80$. Therefore, this wave is considered to be almost a standing wave, because $\lambda_\perp\gtrsim L_x$ and the LHR layer is not in the system. In the higher density region, the lower frequency waves decrease in amplitude and only the higher frequency waves exist, because the LH wave has a property that the higher its frequency is, the higher density the LHR layer and the turning point T_p exist at. The profiles of the amplitude of the pump waves correspond to those of the interferogram $\phi_{cm}(x,t)$.

4.2. Energy deposition on ion and cascade ion tail formation for Run 1

Figures 7(a) and 7(b) show the x-dependent increase in the ion perpendicular and parallel energies at t=40T, where these values were calculated in the 12 regions (see Sec. 3 or Ref. [13]). Figure 8 shows the ion perpendicular velocity distributions, which was calculated in the 4 regions specified by 1-3, 4-6, 7-9, and 10-12, in correspondence with Fig. 7 (see Ref. [13]). The perpendicular kinetic energy per an ion increases by 60~100 % in each region, as shown in Fig. 7(a). A peak increase is seen in the region 8 where a part of main modes (m=7, 8, and 9) have their turning points T_p (see Tab. 4).

Figure 8 indicates that the high energy tail is formed in each region with the significant increase of the bulk temperature. It is noted that Fig. 8 just shows a rough measure of the increase

of the bulk temperatures and profiles of the high energy tail. Therefore, we calculated how much the perpendicular kinetic energy increased below and above $v_{i\perp}^2/2v_{Ti0}^2=v_{Tic}^2=10.2v_{Ti0}^2$ where $v_{i\perp}^2/2v_{Ti0}^2$ stands for $v_x^2/v_{Ti0}^2=v_y^2/v_{Ti0}^2$, exactly to say, U^2/v_{Ti0}^2 in Eq. (26) in Ref. [14]. The position of v_{Tic} is shown by an arrow in Fig. 8. The increase below v_{Tic} can be considered to correspond to that in the bulk temperature, while the increase above v_{Tic} to that in the kinetic energy due to the high energy tail. Within the error of 10 %, we obtained the results in the 4 regions of 1-3, 4-6, 7-9, and 10-12; the bulk temperatures increase by 46 %, 42 %, 37 %, and 29 % and the perpendicular kinetic energies due to the high energy tail increase by 25 %, 36 %, 64 %, and 45 % , respectively. The energy increase near $v_{i\perp}^2/2v_{Ti0}^2=v_{Tic}^2$ is significant compared with that above $v_{i\perp}^2/2v_{Ti0}^2\sim 4v_{Tic}^2$.

The deposit of the wave energy on the perpendicular ion energy is maximum in the region 10-12. The ratios of them are unity in the region 10-12, 0.96 in the region 7-9, 0.43 in the region 4-6, and 0.21 in the region 1-3.

The ion tail density is the largest in the region 7-9 and its population to the bulk ions is 0.027. The turning points T_p of the modes for m=5~11 exist in this region 7-9 (see Tab. 4). These will be discussed in Sec. 5 again.

Ion perpendicular velocity distribution can be approximated by the two Maxwell distribution, and its time variation is as follows; initially the tail with a low temperature is formed, by degrees the tail temperature increases, and after the saturation of its increase the tail density continues to increase. This ten-

dency is similar to the case of the single mode excitation [13].

Now, we consider the correlation between the high energy tail formation of ion and the damping of the waves for each mode, whose interferograms are expressed as $\phi_{cm}(x,t)$, as mentioned in Sec. 4.1. The calculation based on the linear theory predicts no damping before T_p, however, the observed waves for the higher $k_{\parallel m}$ modes are subject to the spatial damping, while the very low $k_{\parallel m}$ ones are not subject. Why only the higher $k_{\parallel m}$ modes are damped against the theoretical prediction? This can be understood as follows; the LH wave has a property that $k_{\perp mr}$ of the wave for higher m becomes larger than that of the wave for lower m, as seen from Fig. 4. In addition, the observed $k_{\perp mr}$ become very large near T_p. The higher $k_{\perp mr}$ modes have the very low perpendicular phase velocities, which are nearly the initial maximum ion velocity in the system. In this case, the ion with high velocity can interact with these modes and can be accelerated by them. Actually, we have observed that the density of the high energy tail of ion is maximum in the region 7-9 where T_p of the higher $k_{\parallel m}$ modes exist. Such an acceleration mechanism may be attributed to the nonresonant stochastic acceleration [8,14].

This theory, however, is on the basis of the monochromatic wave with the constant wave amplitude and the constant $k_{\perp m}$. Therefore, we cannot make a direct comparison between the theoretical prediction and simulation results in this run. Using the spatial averaged quantities, however, we will extrapolate this theory to discuss the phenomena observed in this run in the following.

With respect to the condition (v) presented in Sec. 2, we show the normalized amplitudes for modes m=7 and 9 in the regions 1-3, 7-9,

$$a_{m=7} = 0.09,\ a_{m=9} = 0.12 \text{ in the region 1-3,}$$
$$a_{m=7} = 0.35,\ a_{m=9} = 0.27 \text{ in the region 7-9.}$$

In the region 1-3, $a_{m=7}$ and $a_{m=9}$ are much smaller than the threshold value, 0.25, predicted by Karney [8], while in the region 7-9 $a_{m=7}$ and $a_{m=9}$ are larger than that. It is suggested that the condition (v) is qualitatively valid (see Fig. 8).

Next, we consider the condition (iv). For the nonresonant stochastic acceleration to occur, the condition of $v_{i\perp} > \omega_0/k_{\perp m}$ must be satisfied. The maximum $v_\perp$ of ion at the initial state is about $4(2)^{1/2}v_{Ti0}$, therefore, no particles cannot satisfy initially the condition (iv) for main modes of m=6, 7, 8, and 9. For the higher $k_{\parallel m}$ modes of $m \geq 11$, however, some particles can satisfy the condition (iv). Therefore, these higher modes are damped, so that they make a small number of the highly accelerated particles which satisfy the condition (iv) even for the lower modes, for example, m=8 and 9 (a part of the main modes). These particles interact with those lower modes and damp them, so that they are further accelerated. This process is being iterated. The waves damp successively from the higher modes to the lower modes as explained in Sec. 4.1, and correspondently the ion perpendicular high energy tail is formed step by step.

In other words, this phenomenon may be represented in terms of the velocity space diffusion caused by the multi-mode wave. Let D_m represent the diffusion coefficient due to a

monochromatic wave for mode m and assume that D_m has a finite value enough to diffuse ions within a perpendicular velocity space region R_m where the particle trapping effects and/or stochastic effects are significant, i.e., $R_m=(v_m^{(1)},v_m^{(2)})$ around a perpendicular phase velocity $v_{ph\perp m}$. As the first order approximation in the case of the multi-mode wave, we may assume that the entire diffusion coefficient is represented with the linear summation of D_m, that is, $D=\sum_m D_m$. If the regions R_m and R_{m+1} are overlapped, then ions existing in R_m are expected to be accelerated into R_{m+1} and if not, then no or few ions are. Here, we estimate R_m following Ref. [9]. If the condition (v) mentioned in Sec. 2. is satisfied, R_m is mainly separated into two regions with different physical properties, i.e., $R_m^{(1)}=(v_m^{(1)},v_m^{(s)})$ and $R_m^{(2)}=(v_m^{(s)},v_m^{(2)})$. In the former region, the particle trapping effects are significant and D_m is constant approximately. Here, $v_m^{(1)}\sim v_{ph\perp m}-(e\phi_m/m_i)^{1/2}$ and $v_m^{(s)}\sim v_{ph\perp m}+(1/2(\Omega_i/k_{\perp m})^2 v_{ph\perp m})^{1/3}$, respectively. In the latter region, the stochastic effects are significant and D_m with complex expression decreases slowly with $v_\perp$ approximately [9]. Therefore, the upper limit of the region $R_m^{(2)}$, i.e., $v_m^{(2)}$ is very widely streched and is not so definitely determined. If the condition (v) is not satisfied, $D_m=0$. Here, let us apply this consideration to the results for Run 1. In the case of ions existing in the region 7-9, the modes for $m\geq 5$ satisfy the condition (v) and $R_m^{(1)}$ for $m\geq 5$ are overlapped, while the modes for $m\leq 4$ do not satisfy the condition (v) and have $D_m=0$. In the case of the mode for m=5, $v_{ph\perp m}/v_{Ti0}=9.4$ and $v_m^{(s)}/v_{Ti0}=11.6$. By a careful examination of the observed ion velocity distribution, it is found that the maximum perpendicular

velocity of ion is about $14v_{Ti0}$ and that this maximum velocity is included in the region $R_{m=5}$ [2]. When each region R_m is overlapped with its neighbor, therefore, ions are diffused successively from the lower velocity to the higher velocity through the overlapping region.

Figures 9(a) and (b) show the x-dependent increase in the electron perpendicular and parallel energies at t=40T. The perpendicular one slightly increases, while the parallel increase shows the significant surface heating as well as the case in Run 2. The mechanism is the same as that discussed in Sec. 4.5.

4.3. Effects of the ponderomotive force on the plasma

Figure 10(a) and (b) show the difference between the initial electron density and the density temporally averaged from t=0 to 40T and the ion perpendicular drift current averaged during the time between t=31.5T and 37.8T which corresponds to an ion cyclotron period. As shown in Fig. 10(a), the density depression is formed along the propagation cone of the LH wave due to the parallel ponderomotive force on the electrons. Its magnitude $\delta n_e/n_{e0}$ is stronger in the lower density region than in the higher density region and its maximum reaches 0.25 in front of the antenna. Its value roughly agrees with a theoretical estimate [20], given by

$$\frac{\delta n_e}{n_{e0}} = -\frac{\varepsilon_0 \langle |E|^2 \rangle}{2n_{e0}(T_e+T_i)} \sim -0.22 \qquad (26)$$

where the bracket $\langle\ \rangle$ means the time average.

The perpendicular ponderomotive force is important as well as the parallel ponderomotive force, that is, the latter causes density depression, while the former influences the ion diamagnetic drift. Particles are subject to the perpendicular ponderomotive force given by [20],

$$\vec{F}_{p\perp\sigma}=-\frac{\partial}{\partial x}\left[\left(\frac{\omega_{p\sigma}\omega_0}{\omega_0^2-\Omega_\sigma^2}\right)^2\frac{\varepsilon_0<|E_x|^2>}{2}+\frac{\omega_{p\sigma}^2}{\omega_0^2-\Omega_\sigma^2}\frac{\varepsilon_0<|E_z|^2>}{2}\right]\hat{x} \quad , \tag{27}$$

where σ stands for electron or ion. This force causes the following additional perpendicular drift to the usual diamagnetic drift,

$$v_{Dp\sigma}=\frac{\vec{F}_{p\perp\sigma}\times\vec{B}_0}{e_\sigma B_0^2}=-\frac{F_{p\perp\sigma}}{e_\sigma B_0}\hat{y} \quad . \tag{28}$$

In the case of the LH wave, Eq. (27) can be approximated for ions and electrons as follows;

$$v_{Dpi}\sim\frac{1}{eB_0}\frac{\partial}{\partial x}\{(\omega_{pe}/\omega_0)^2\varepsilon_0<|E|^2>/2\} \quad , \tag{29}$$

$$v_{Dpe}\sim\frac{-1}{eB_0}\frac{\partial}{\partial x}\{(\omega_{pe}/\Omega_e)^2[(\omega_0/\Omega_e)^2\varepsilon_0<|E_x|^2>/2-\varepsilon_0<|E_z|^2>/2]\} \quad . \tag{30}$$

Figure 10(b) indicates that ion drift expressed by Eq. (29) significantly exceeds the diamagnetic drift around the propagation cone in the high density region, that is, it enhances or cancels the diamagnetic drift. Therefore, its drift may be considered to influence the suppression or the enhancement of the drift wave significantly [33-35]. In the case of this simulation, however, this phenomenon cannot be studied furthermore, because the elec-

tric polarization of the y direction, that is, the coupling of the particle motion in the y direction with the field is neglected in the used simulation model [13].

4.4. Wave propagation for Run 2

Figure 11 shows the interferogram $\phi_{cm}(x,t=12T)$ for m=5, 7, and 9. Each ϕ_{cm} is normalized by the surface electron temperature, $T_{e0R=1}$. It should be noted that the electron temperature is set increasing exponentially with x for Run 2 (see Sec. 4.1.). As shown in Fig. 11, therefore, the waves for m=7 and m=9 are subject to the electron Landau damping in the high density region and damp more strongly near T_p compared with those in Run 1. The amplitude of the wave source is smaller than that in Run 1 in order to decrease the surface current. These situations lead to an inclination of larger influences of the thermal fluctuations on the interferogram ϕ_{cm} compared with those in Run 1. In addition, side band waves with large amplitudes, which will be shown later, influence on the interferograms. As shown in Fig. 12, therefore, $k_{\perp mr}$ calculated from the interferograms are considerably scattered around the theoretical values. For the mode of m=9, the theoretical imaginary part of $k_{\perp m}$, $k_{\perp mi}$ becomes finite near a point of $v_{ph\#m}/v_{Te0}=3.5$ before T_p and increases smoothly compared with that in Run 1, which is free from the electron Landau damping.

Only cold modes are shown in Fig. 12, because in the case of the large dissipation the cold mode does not intersect the hot mode and the mode conversion is difficult to occur [36].

Figure 13 shows the wave spectra for m=3, 5, and 9. We can see that many side band waves grow and that their amplitudes are almost as large as that of the pump wave. Their frequencies are $\omega_s=\pm 2.3\omega_0$ for m=5, $\omega_s=-2.5\omega_0$ for m=7, and $\omega_s=\pm 2.14\omega_0$ for m=9. In each case, the frequency is too high for the wave to be subject to the electron Landau damping. These waves are the LH modes as well as those seen in Run 1.

Because the observed perpendicular wave lengths are long, that is, $\lambda_\perp \sim 1/4 \sim 2L_x$ and their LHR layers do not exist because of $\omega_s > (\omega_{LH})_{max}=10\Omega_i$, these side band waves become standing waves due to the reflection on the wall. In the wave spectra, actually, the jumps of phases by about π which imply that these are almost standing waves can be observed at positions where the amplitudes of the side band waves become considerably small (see Fig. 13). One of these positions is near T_p for each mode in contrast with that in Run 1. The phase variation between succesive phase jumps implies that, with respect to m=5, the phase velocity is directed toward the higher density region. In the case of the backward waves such as the LH waves, therefore, the waves are considered to be excited in the higher density region and propagate to the lower density region. In the cases of the m=7 and 9, the phase variation is so disturbed that the direction of the phase velocity cannot be identified.

4.5. Increase of the kinetic energy of plasma for Run 2

Figures 14(a) and (b) show the increments of the parallel and perpendicular kinetic energies per an electron, respectively.

Figures 15(a) and (b) show the same quantities for ion.

As shown in Fig. 14(a), the increment of the parallel kinetic energy for the electron strongly depends on x, that is, electrons at the plasma surface gain large parallel kinetic energy in accordance with the current generation shown later, while electron at the higher density region are cooled considerably. In the following, we will examine their mechanisms.

The surface heating is considered to be caused by the particle trapping caused by the localized intense wave, and/or by the transit time heating. These two mechanisms may be reduced to or correlated with the Landau damping in the limit of the small wave amplitude. In the region 1-3 which is the plasma surface, finiteness of their wave amplitude cannot be negligible. Now, we will examine these mechanisms in the results of this run.

Let the parallel wave number of a typical wave which forming the propagation cone be $k_{\parallel m}^{*}$, in this case, the electrons resonant with this typical wave transit the propagation cone with width of Δz during an autocorrelation time $\tau_{ac}=\Delta z/(v_{ph\parallel}-v_{g\parallel})$, where $v_{ph\parallel}=\omega_0/k_{\parallel m}^{*}$ and $v_{g\parallel}=\partial\omega_0/\partial k_{\parallel m}^{*}$. When we define the trapping time as $\tau_{tr}=2\pi(e\phi k_{\parallel m}^{2}/m_e)^{-1/2}$ and choose one of the main modes, i.e., the mode for m=7, as the typical wave, then we obtain $\tau_{ac}/\tau_{tr}\sim 0.5$. Therefore, the trapping effect of the resonant particles may be significant [37].

Because it takes about 12T for electrons with the parallel velocity $3v_{Te0}$ existing at the plasma surface to circulate the system along z, the waves oscillate many times during the time when the electrons escaping the cone reenter it. This corresponds to a condition for the phase randomization. In addition, as the

maximum energy increment obtained at one transit is so large that $\Delta v_{max}/v_{Te0}=(eE/m_e\omega_o)/v_{Te0}$ is order unity where Δv_{max} indicates the maximum velocity which an electron can acquire in each passing of the propagation cone. Therefore, the validity of the transit time heating for this simulation result is supported by these facts: (i) the phase randomization and (ii) the large acceleration by the localized wave [38,39]. Therefore, this heating mechanism is considered to be significant for this system, as well as the trapping effects.

Provided that we change the physical view point, that is, we consider a localized wave as a sum of the many modes with the different parallel phase velocities, we can explain this phenomenon in the following way. A wave with the the parallel phase velocity $v_{ph\parallel m}$ forms an island, in which the electrons are trapped and the width of which is defined as $2(e\phi_m/m_e)^{1/2}$ [29]. Estimating the wave amplitude from the interferogram $\phi_{cm}(x,t)$, we know that the islands are overlapping for $m\geq 4$ and not for $m\leq 3$. The upper boundary of the island for m=4, $v_{ph\parallel m}+ 2(e\phi_m/m_e)^{1/2}$, is about $10.1v_{Te0R=1}$ and this value corresponds to the maximum parallel velocity of electrons which is seen in the velocity distribution of the electron in the region 1-3, likely as the cascade formation of the high energy tail mentioned in Sec. 4.2. Correspondently, the wave for m=3 does not damp before T_p as seen from the interferogram $\phi_{c3}(x,t)$.

As the velocity diffusion coefficient may increase with the wave amplitude, the lar r the wave amplitude is, the larger electron current and heating it results in, and the stronger the wave damping is there. In the case of the high wave amplitude, this

mechanism leads to an inclination of formation of the surface current rather than the body current.

The mechanism of the decrease in energy in the higher density region can be attributed partly to the collisional relaxation between the electrons and ions because $T_{e0max}/T_{i0}=4.8$. Furthermore, we should take a caution against the spatial variation of the electron temperature which is initially set. The cross-field energy transport can occur by the electron-electron collision. In addition, the following mechanism enhances it: the cross-field electron energy transport due to the electron plasma waves which are excited in the higher temperature region may play a role because the electron Landau damping is significant in the higher temperature region. This mechanism is related only to the parallel energy transport [40] and so may explain the larger decrease of the parallel kinetic energy than the perpendicular kinetic energy as shown in Figs. 14(a) and (b).

The perpendicular kinetic energy increase of the ion is mainly due to the LH wave. The increment is small compared with that in Run 1, because the energy of the LH wave deposits mainly on electrons and the source amplitude is lower. When ions with large Larmor radii, that is, high velocities reach the left limiter, they are cooled in average against some energy increase due to the direct acceleration by the wave, because they are reflected in the system with the velocities whose deviation is the initial thermal velocity. This leads to the decrease of the ion perpendicular kinetic energy in the region 1, as shown in Fig. 15(b).

4.6. Electron current profile and parallel velocity distribution for Run 2

Figure 16 shows the electron mean parallel velocity V_e and current J_e at t=66T. As shown in Fig.11(c), the waves for $m \gtrsim 8$ damped in the region 4-6 before their turning points T_p shown by arrows in Fig. 16, because the Landau damping is significant there. These wave dampings lead to the current generation. The current generated in the region of $x \gtrsim 64$ is due to the waves for $m \gtrsim 7$, which penetrate with small amplitudes beyond their turning points T_p. The waves for $m \lesssim 6$ can slightly contribute to the current generation in this region, because their phase velocities are too fast to interact with the electron, for example, $v_{ph\|m}/v_{TeOR=7}=3.9$ for m=6.

Figure 17 shows the time variation of V_e and J_e in the region 4-6. The current increases almost linearly with time. The symptom of the saturation has not been observed yet. This implies that the system does not reach the steady state.

Here, we examine the electron parallel velocity distributions, the first order moments of which are proportional to the current J_e. Although the velocity distribution has not reached the steady state yet, it seems insignificant to continue this run furthermore, because the parameters of the plasma has changed so much, especially, the electron temperature in the region 12 has decreased by about 35 % at t=66T.

Assuming that the plasma parameters remain as it is at t=66T, we obtain a velocity distribution of the steady state as a theoretical approximation. Although this assumption is not so

valid for the time scale when the velocity distribution reaches the steady state in this run, we want a rough measure which may evaluate the intermediate state of the velocity distribution approximately. For this purpose, we use Eq. (16), which is derived by the simple theoretical consideration. As the value of each potential ϕ_m in the diffusion coefficient D_m, the observed interferogram ϕ_{cm} is substituted. The collision frequency ν_c in D are adjusted so as to fit the numerical calculation of Eq. (16) to the observed distribution at t=66T.

We consider the wave damping in the region 4-6. The waves for m<5 little damp there, because their parallel phase velocities are so high that few electrons can interact with these modes. We calculated two curves in the cases that the waves for m≤5 and for m≤4 are included, respectively, as shown in curves a and b in Fig. 18. The collision frequency ν_c is chosen to be about $40\omega_0$ as a result. This leads to D=O(0.1).

As discussed in Sec. 4.5, the interactions between the wave and the electron progresses by degrees from its higher $k_{\parallel m}$ modes to the lower ones and the formation of the high energy part of the velocity distribution delays compared with that of the low energy. Therefore, the state at t=66T in Fig. 18 seems to mean that the interaction between the mode for m=4 and the electron begins but does not reach its steady state. At this time, correspondently, we observed some damping of the mode for m=4 compared with that at t=12T. In contrast, we cannot observe any damping of the mode for m=3 even at this time.

5. DISCUSSION AND CONCLUSION

We performed several runs in which preliminary runs were included, and chose two typical runs from them, and analyzed their results in detail in order to investigate the ion heating and current generation due to the LH wave emitted from the finite-length antenna. Simulation parameters were set so that the wave energy deposited mainly on ions for Run 1 and on electrons for Run 2. We will summarize the obtained results and indicate the relation between these simulation results and other works concerning the physical problems on the ion heating and the electron current generation. In addition, we will discuss the problems remained in the future.

The LH wave excited by the finite-length antenna forms the propagation cone and travels from the low density region to the high density region. Up to the LHR layer, its trajectory well agrees with the characteristic curve obtained using the cold plasma approximation and the WKB method.

Two nonlinear phenomena due to the ponderomotive force were observed along this propagation cone. The density depression is clearly observed in front of the antenna at the low density region. Its magnitude is not so large that it does not influence the wave propagation. The maximum $\delta n_e/n_{e0}$ is about 25 %. This value well agrees with a theoretical estimation Eq. (26). On the other hand, the ion cross-field drift is conspicuous rather in the high density region. Its magnitude is enough large to change the direction of the original diamagnetic drift of ion. Therefore, it is possible to relate this drift with the enhancement or the sup-

pression of the drift instabilities [33-35]. As mentioned in Sec. 4.3, the influences of this cross-field drift by the spatially localized wave on the drift waves and plasma diffusions are remained as the future problems.

Changing the physical view point, we investigated the wave propagation, that is, the dependence of each Fourier-expanded mode with respect to the z (periodical) direction on x, t in detail. The lower $k_{\parallel m}$ modes neither damp nor interact with the particles. Their real parts of $k_{\perp m}$, $k_{\perp mr}$ well agree with those from the linear theory up to the turning point T_p. Because a reflected mode was observed, the mode conversion from the cold mode to the hot mode [6] was expected to occur. Its reflected wave, however, was identified to be a cold mode. The collision of $\nu_c/\omega_0 \sim 5\times10^{-4}$ may prevent the mode conversion [12]. Collisional effects in this run are larger at least than those corresponding to this value. To the best knowledge of the authors, however, neither the observations nor the theoretical predictions on the reflection of the cold mode has not been reported yet. For the theoretical calculation of the mode conversion, one has assumed existence of only the incident cold mode and the reflected hot mode near the turning point [6,12]. However, we should point out a necessity of inclusion of the reflected cold mode to them. If the amplitude of the reflected cold mode is concluded to vanish theoretically, it is necessary to take the influence of the right wall into the consideration as a higher order effect in this simulation. We think that this possibility is little.

In the case of the higher $k_{\parallel m}$ modes, we have also observed interesting phenomena: against the prediction from the linear

theory, the waves damped almost uniformly in space. Furthermore, its observed $k_{\perp mr}$ does not agree with the prediction from the linear theory near the turning point . Lost wave energy corresponding to the damping of the higher $k_{\parallel m}$ modes deposits mainly on ions in the form of the increase in the perpendicular kinetic energy for Run 1. In paticular, its increase is connected with the high energy tail. This ion acceleration mechanism is explained qualitatively as the nonresonant stochastic acceleration [8,14]. Rigorously speaking, however, this theory is concerned with the case of the monochromatic wave and , therefore, it cannot be applied simply to the multi-mode wave such as the localized wave.

Here, we will summarize the important phenomenon concerning the multi-mode wave. The higher $k_{\parallel m}$ modes with considerably smaller amplitude compared with the main modes play key roles on this phenomenon. Some of them accelerate a small number of ions with the high velocities around their perpendicular phase velocities. Accelerated ions become able to interact with the lower $k_{\parallel m}$ modes compared with the above ones, that is, the modes with the higher perpendicular phase velocities and are accelerated a little furthermore by them. This process is iterated. Eventually, these accelerated ions become able to interact with main modes with the large amplitudes and are accelerated furthermore. Against theoretical calculation, main modes damp in space due to loss of their energy to ions. Namely, the interaction between each Fourier-expanded mode and ions progressed in a manner of formation of the cascade from the higher $k_{\parallel m}$ modes to the lower $k_{\parallel m}$ modes. Therefore, we call this process the cascade formation of

the high energy tail of ion by the multi-mode wave.

We observed the significant increase in the bulk temperature of ion for Run 1. The maximum wave amplitude is $(e\phi/T_{i0})_{max}=28$. Even if the monochromatic wave, for example, one corresponding to the mode for m=8, has this wave power, the condition of the bulk heating is not satisfied at all so long as we judge according to Eq. (29) in Ref. [14]. Therefore, some other mechanisms about the increase in the bulk temperature are considered: effects associated with the multi-mode wave, collisional effects, effects of the low-frequency side band waves with frequency near Ω_i [15]. These mechanisms are expected to work together. It should be noted that the wave energy deposits on the high energy tail more than on the bulk as a whole, because the bulk temperature increase is localized near the plasma surface.

For Run 2 it was observed that the electron current flowed more in the lower density region than in the higher density region. This surface current is not expected from the linear theory. Obviously, the wave amplitude was too strong to form a body current. If the waves are subject to damping at the plasma surface due to some nonlinear mechanisms stronger than that due to linear ones, the waves damp before reaching the plasma center in the case of the LH wave. Therefore, the surface current is inevitably formed when the wave amplitude is considerably high. In order to avoid the surface current, we should decrease the wave amplitude and/or increase the frequency of the pump wave so as to put the LHR layer out of the plasma. When we can decrease the wave amplitude by one order of magnitude compared with Run 2, we may expect to observe generation of the body current. However, it

is very much expensive to perform such a run only for proof of this by the use of the today's available computer.

As a second approach, we can try to increase the frequency and the parallel phase velocity of the pump wave. Because this causes to put the LHR layer out of the plasma, the LH wave penetrates the plasma and is subject to some reflection on the wall. Through this process, electrons mainly absorb the wave momentum and energy due to the electron Landau damping. For this simulation, we need to change the presently used model. This is a problem remained in the future.

Finally, we will mention about the availability of this simulation model. Using both the elongated grid and the quadric spatial interpolation, we can deal with the system about 10 times larger than that in the usual model. This method or the further improved one, therefore, is considered to be useful for other simulations on the fusion plasma and may lead to increase in the potentiality of the particle simulation in the research of the nuclear fusion field.

ACKNOWLEDGMENTS

The authors wish to express their gratitude to Dr. N.J.Fisch for his useful discussions. The authors also thank Prof. S.Tanaka and Dr. G.J.Morales for their interests to this work and some discussions. One of the authors (N.N.) expresses his deep appreciation to Prof. H.Momota for supporting this work and some discussions. He is also grateful to Dr. H.Naitou and K.Satou for the discussion about physical consideration.

This work was partially supported by the Grant-in-Aid for Scientific Research of the Ministry of Education, Science and Culture in Japan and has been carried out under the Collaborating Research Program at the Institute of Plasma Physics, Nagoya University.

REFERENCES

[1] PORKOLAB, M., S. BERNABEI, B., HOOKE, W.M., MOTLEY, R.W., NAGASHIMA, T, Phys. Rev. Lett. 38(1977) 230.

[2] SCUSS, J.J., FAIRFAX, S., KUSSE, B., PARKER, R.R., PORKOLAB, M., GWINN, D., HUTCHINSON, I., MARMAR, E.S., OVERSKEI, D., PAPPAS, D., SCATURRO, L.S., WOLFE, S., Phys. Rev. Lett. 23(1979) 274.

[3] NAGASHIMA, T., FUJISAWA, N., Proc. of Joint Varrenna-Grenoble Int. Sympo. on Heating in Toroidal Plasma, edited by CONSOLI, T. and CALDIROLA (Pergamon, Elmsford, N.Y., 1979), Vol. II, P. 281.

[4] BRIFFOD, G., - WEGA AND PETULA TEAMS, Proc. of the Int. Conf on Plasma Physics, Session 10A-4 (Nagoya, Japan, Apr., 1980).

[5] YAMAMOTO, T., IMAI, T., SHIMADA, M., SUZUKI, N., MAENO, M., KONOSHIMA, S., FUJII, T., UEHARA, K., NAGASHIMA, T., FUNAHASHI, A., FUJISAWA, N., Phys. Rev. Lett. 45(1980) 716.

[6] STIX, T.H., Phys. Rev. Lett. 15(1965) 878.

[7] BRAMBILLA, M., Nucl. Fusion 16(1976) 47.

[8] KARNEY, C.F.F., Phys. Fluids 21(1978) 1584.

[9] KARNEY, C.F.F., Phys. Fluids 22(1979) 2188.

[10] FISCH, N.J., Phys. Rev. Lett. 41(1978) 873.

[11] KARNEY, C.F.F., FISCH, N.J., Phys. Fluids 22(1979) 1817.

[12] BELLAN, P.M., PORKOLAB, M., Phys. Fluids 17(1974) 1592.

[13] ABE, H., ITATANI, R., MOMOTA, H., Phys. Fluids 22(1979) 1533.

[14] ABE, H., MOMOTA, H., ITATANI, R., FUKUYAMA, A., Phys. Fluids 23 (1980) 2417.

[15] ABE, H., Inst. of Plasma Physics of Nagoya Univ. Rep. IPPJ-476(1980)

[16] DECYK, V.K., DAWSON, J.M., MORALES, G.J., Phys. Fluids 22(1979) 507.

[17] DECYK, V.K., MORALES, G.J., DAWSON, J.M., Phys. Fluids 23(1980) 826.

[18] DECYK, V.K., MORALES, G.J., DAWSON, J.M., Univ. of California, Los Angeles Rep. PPG-517 (1980).

[19] MATSUDA, K., MATSUDA, Y., GUEST, G.E., Phys. Fluids 23(1980) 1422.

[20] MORALES, G.J., LEE, Y.C., Phys. Rev. Lett. 35, 930.

[21] OKUDA, H., LEE, W.W., CHENG, C.Z., Princeton Plasma Physics Laboratory Report PPPL-1461 (1978)

[22] LEWIS, H. R., SYKES, A., WESSON, J.A., J. Comput. Phys. 10(1972) 85.

[23] BROWN, D.I., GITOMER, S.J., LEWIS, H.R., J. Comput. Phys. 14(1974) 193.

[24] ABE, H., MIYAMOTO, J., ITATANI, R., J. Comput. Phys. 19(1975) 134.

[25] LANGDON, A.B., J. Comput. Phys. 6(1970) 247.

[26] ABE, H., Dr. Thesis, Kyoto Univ. (1976).

[27] Kuehl, H.H., Ko, K.K., Rhys. Fluids 18(1975) 1816.

[28] ABE, H, NAITOU, H, ITATANI, R, J. Phys. Soc. Jpn 41(1976) 1364.

[29] STIX, T.H., Weizmann, Proc. of Joint Varrenna-Grenoble Int. Sympo. on Heating in Troidal Plasma, edited by CONSOLI, T. and CALDIROLA (Pergamon, Elmsford, N.Y., 1979), Vol. II, P. 363.

[30] BIRDSALL, C.K., FUSS, D., J. Comput. Phys. 3(1971) 494.

[31] NAITOU, H., TOKUDA, S., KAMIMURA, T., J. Comput. Phys. 33(1979) 86.

[32] ICHIMARU, S., Basic Principles of Plasma Physics (Benjamin, New York, 1973).

[33] AINBERG, YA. B., SHAPIRO, B. D., Zh. Eksp. Teor. Fiz. 52(1966) 293 [Sov. Phys. JETP 25(1967) 189].

[34] GORE, R., GRUN, J., LASHINSKY, H., Phys. Rev. Lett. 40(1978) 1140.

[35] BELLAN, P.M., WONG, K.L., Phys. Fluids 21(1978) 841.

[36] SIMONUTTI, M.D., Phys. Fluids 18(1975) 1524.

[37] DAVIDSON, R.C., Methods in Nonlinear Plasma Theory (Academic press New York, 1972).

[38] SUGAI, H., IDO, K., TAKEDA, S., J. Phys. Soc. Jan 46(1979) 228.

[39] MORALES, G.J., LEE, Y.C., Phys. Rev. Lett. 33(1974) 1534.

[40] NAITOU, H., J. Phys. Soc. Jan 48(1980) 608.

TABLE I. SIMULATION PARAMETERS

Run no.	1	2
Mass ratio : m_i/m_e	100	100
Pumping frequency : ω_0/Ω_i	6.3	5.4
Max($e\phi/<T_{e0}>$) in vacuum	7.0	2.1
Max($e\phi/T_{e0min}$) in vacuum	7.0	5.0
No. of spatial grids : $M_x \times M_z$	128×256	128×256
Ratio of the grid lengths : $\Delta z/\Delta x$	8.0	8.0
System size : $L_x \times L_z$	128×2048	128×2048
Antenna length : L_A/L_z	0.125	0.125
Cloud radii : $R_x/\Delta x$, $R_z/\Delta z$	0.67, 0.67	0.67, 0.67
No. of particles :	179200	114688
Maximum density $\omega^2_{pe,max}/\Omega^2_e$	0.75	0.5
and its position x_1	120	120
Minimum density $\omega^2_{pe,min}/\Omega^2_e$	0.1	0.05
and its position x_2	8	8
Position of antenna : x_a	3	3
Position of Left Limiter : ℓ_1	4	4
Position of right limiter : ℓ_2	124	124
Initial ele. temperature ratio : T_{e0max}/T_{e0min}	1.0 (uniform)	4.83 (nonuniform)
Initial ion temperature : T_{i0}/T_{e0min}	0.25(uniform)	1.0 (uniform)
Average Debye length : λ_{De}	0.88	1.73
Initial ele. Lamor radius : γ_{Le0}	0.71	1.08 (average)
Initial ion Lamor radius : γ_{Li0}	3.54	6.92

TABLE II. PARALLEL RESONANT VELOCITIES FOR RUN 1

Mode number	3	4	5	6	7	8	9	10	11	12
$v_{\parallel mr}/v_{Ti0}$	13.0	9.8	7.8	6.5	5.6	4.9	4.4	3.9	3.6	3.3

TABLE III. PHASE VELOCITIES

Mode number	3	4	5	6	7	8	9	10	11	12
$v_{ph\parallel m}/v_{Te\parallel 0}$ for Run 1	13.7	10.3	8.2	6.9	5.9	5.1	4.6	4.1	3.7	3.4
$v_{ph\parallel m}/v_{Te\parallel 0R=1}$ for Run 2	11.8	8.8	7.1	5.9	5.0	4.4	3.9	3.5	3.2	2.9

TABLE IV. THE POSITIONS OF THE TURNING POINTS

Mode number	3	4	5	6	7	8	9	10
T_p for Run 1	99	95	91	87	82	79	74	71
T_p for Run 2	87	82	74	70	61	55	48	43

FIGURE CAPTIONS

Fig. 1

A wave number spectrum for the antenna with $\delta=\pi/2$ and R=8 where $A=\sum_{m=-\infty}^{\infty} A_m(\pi/2,8)$. Each positive m corresponds to the Fourier mode propagating to the positive z direction and vice versa.

Fig. 2

Equipotential lines of the interferogram of the potential for Run 1. Distance to the z direction is scaled down to one sixteenth compared with that to the x direction: (a) $\phi_c(x,z,t=4T)$; (b) $\phi_c(x,z,t=12T)$. A bold curve indicates characteristic curve Eq. (8).

Fig. 3

The x-dependent interferograms of the potential for Fourier sin modes, $\phi_{cms}(x,t=12T)$, for Run 1. The symbol T_p denotes the position of the turning point for each mode: (a) for m=3, (b) for m=5, (c) for m=7, and (d) for m=9.

Fig. 4

The perpendicular wave numbers vs. x for Run 1. These are normalized by the parallel wave number of the wave for m=1. The solid lines and the chain lines indicate their real and imaginary parts calculated from the linear dispersion relation, respectively. The plus signs in-

dicate the real parts from the simulation results: (a) for m=3, (b) for m=7, and (c) for m=9.

Fig. 5

The x-dependence of the phase θ_m for Run 1 which is defined as $\mathrm{Tan}^{-1}(\phi_{cmc}(x,t)/\phi_{cms}(x,t))$ where ϕ_{cmc} and ϕ_{cms} are the Fourier cos and sin modes of the interferogram $\phi_c(x,z,t=28T)$, respectively.

Fig. 6

The x-dependent wave spectrum of the potential for each Fouier mode $\phi_m(x,\omega)$ for Run 1. These are calculated during the time between t=0 and 20T. The symbol T_p indicates the turning point of each mode: (a) for m=3, (b) for m=7, and (c) for m=9.

Fig. 7

The x-dependent kinetic energy increases per an ion at t=40T for Run 1: (a) perpendicular component ; (b) parallel component.

Fig. 8

Ion perpendicular velocity distributions at t=40T for Run 1. An arrow indicates v_{Tic}^2 which separates bulk and tail part. A broken line indicates the initial Maxwell distribution.

Fig. 9

The x-dependent kinetic energy increases per an electron at t=40T for Run 1: (a) perpendicular component ; (b) parallel component.

Fig. 10

The phenomena caused by the ponderomotive force:
(a) Contour lines of the constant values of $\delta n_e/n_{e0}$ at t=40T for Run 1. In the regions between limiter and wall, where $n_{e0}=0$, the value $\delta n_e/n_{e0}$ is set 0.
(b) Ion perpendicular current averaged over an ion cyclotron period for Run 1. The direction of an arrow sign parallel to the longitudinal line corresponds to the y directional one, and that parallel to the horizontal line corresponds to the x directional one. The large velocity flow in the y direction near the wall $x=L_x$ is due to the boundary effects which is not influence at all on the observed physical phenomena.
Distance to the z direction is scaled down to one sixteenth compared with that to the x direction.

Fig. 11

The x-dependent interferograms of potential for Fourier sin modes, $\phi_{cms}(x,t=12T)$, for Run 2: (a) for m=5, (b) for m=7, and (c) for m=9.

Fig. 12

The perpendicular wave numbers and parallel phase velocities vs. x for Run 2. The broken lines indicate the parallel phase velocities normarized by the initial electron thermal velocity: (a) for m=5, (b) for m=7, and (c) for m=9.

Fig. 13

The x-dependent wave spectra of the potential for each Fouier mode $\phi_m(x,\omega)$ for Run 2: (a) for m=5, (b) for m=7, and (c) for m=9.

Fig. 14

The x-dependent kinetic energy increases per an electron at t=40T for Run 2: (a) parallel component ; (b) perpendicular component.

Fig. 15

The x-dependent kinetic energy increases per an ion at t=40T for Run 2: (a) parallel component ; (b) perpendicular component.

Fig. 16

Electron parallel drift velocity V_e and electron parallel current J_e vs. x at t=40T for Run 2. Arrows indicate parallel phase velocities of m=10, 9, and 8 located from left side.

Fig. 17

Time variation of the electron parallel drift velocity and electron parallel current in the region 4-6 for Run 2.

Fig. 18

Time variation of the electron parallel velocity distribution in the region 4-6 for Run 2. A curve a indicates the theoretical steady-state distribution which is calculated using the diffusion coefficient Eq. (19) with fourier modes $m \geq 5$, while a curve b is calculated using that with Fourier mode $m \geq 4$. Three arrows indicate the parallel

phase velocities for m=12, 5, and 4 located from the left side.

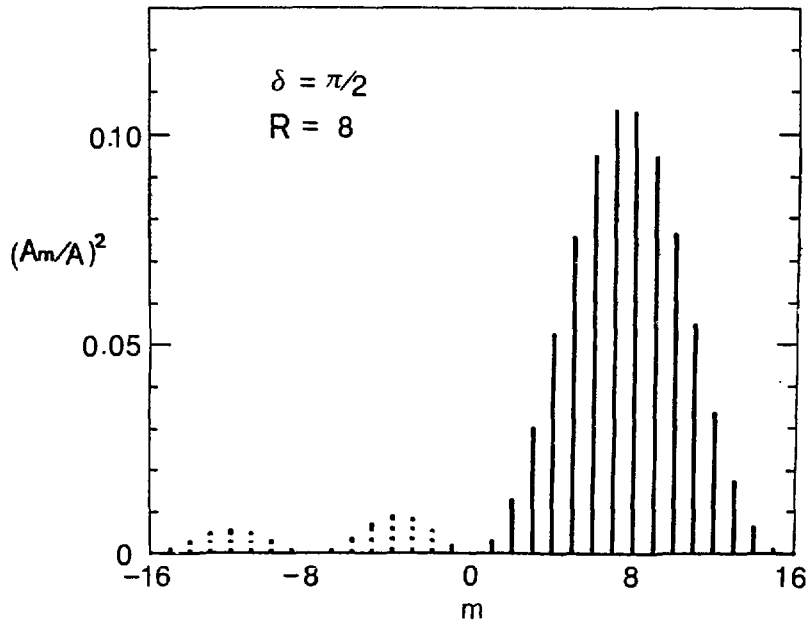

Fig. 1

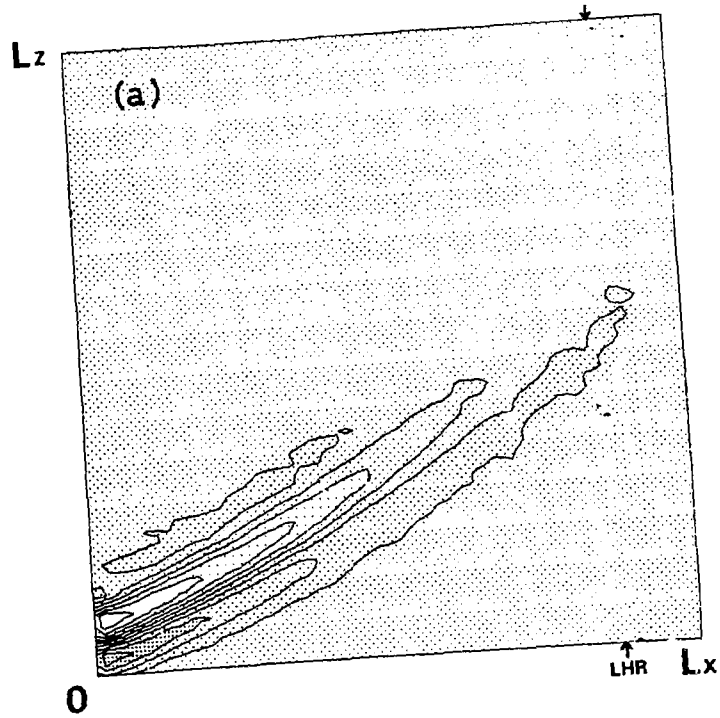

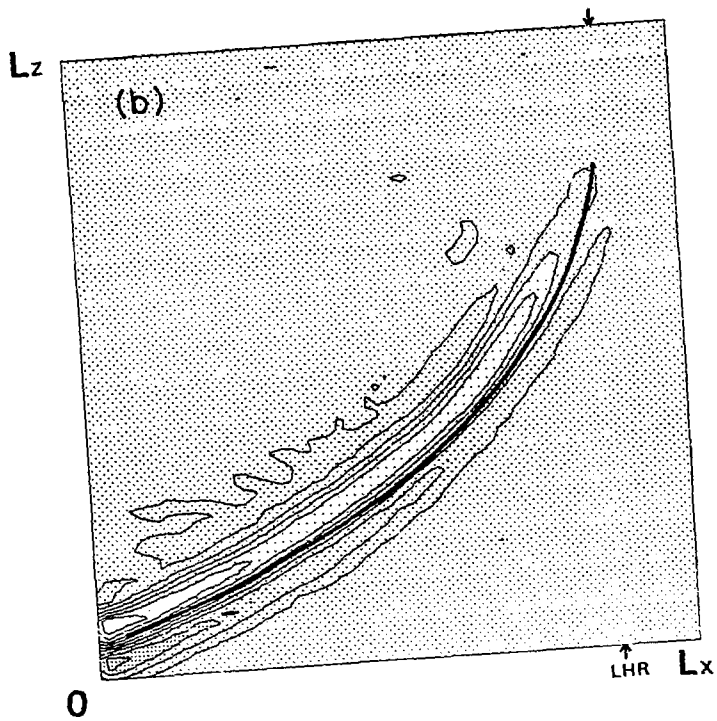

Fig. 2

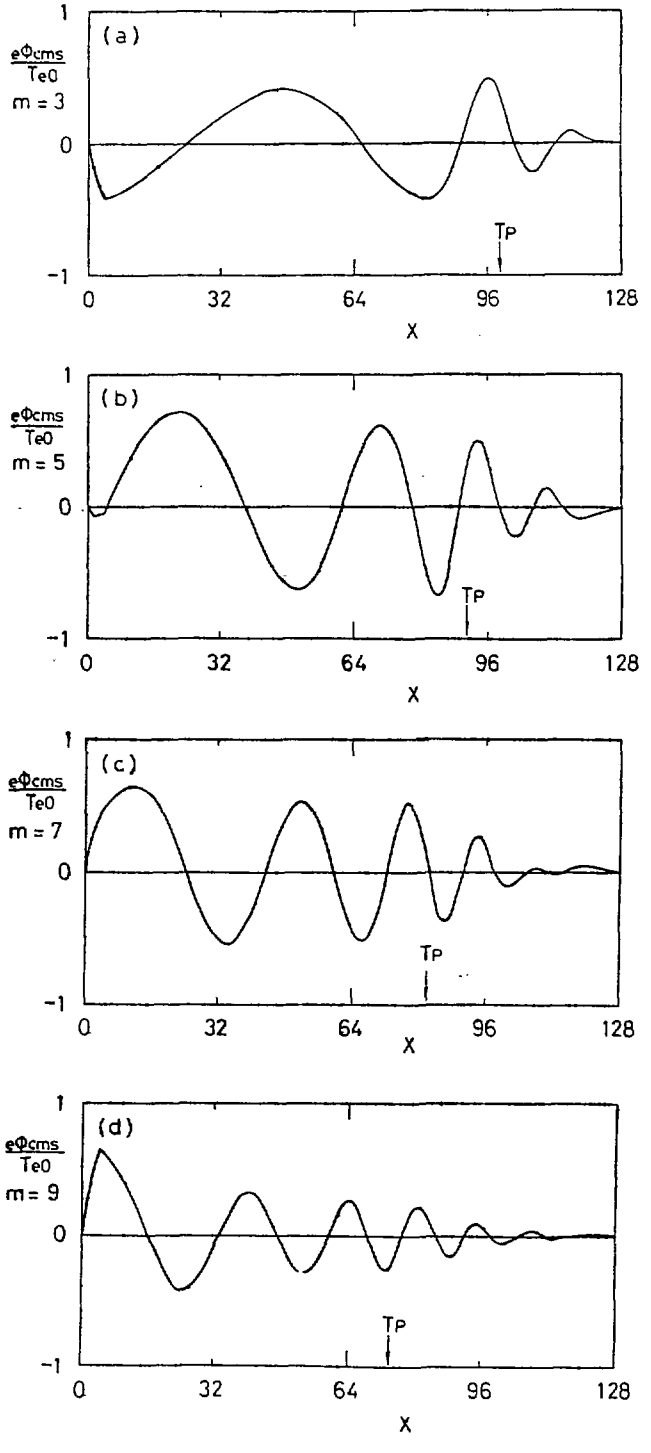
(a)
eΦcms/Te0
m = 3
1
0
-1
Tp
0
32
64
96
128
X
(b)
eΦcms/Te0
m = 5
1
0
-1
Tp
0
32
64
96
128
X
(c)
eΦcms/Te0
m = 7
1
0
-1
Tp
0
32
64
96
128
X
(d)
eΦcms/Te0
m = 9
1
0
-1
Tp
0
32
64
96
128
X

Fig. 3

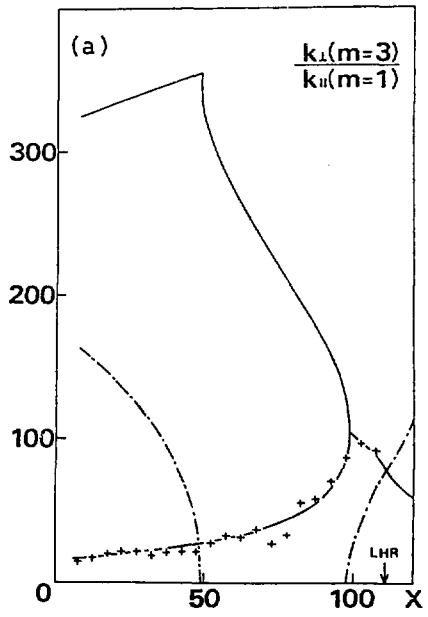
(a)
k⊥(m=3)
k∥(m=1)
300
200
100
0
50
100
X
LHR

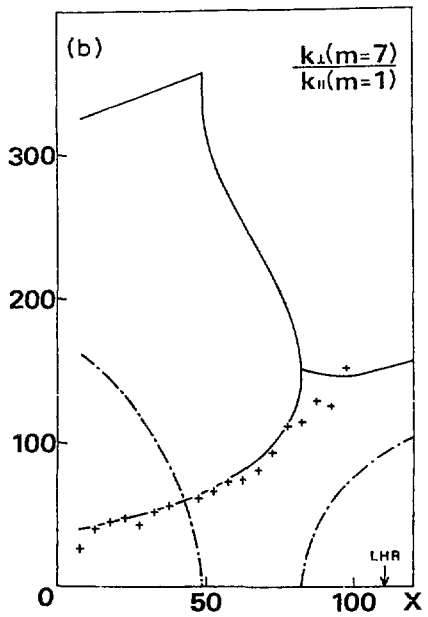
(b)
k⊥(m=7)
k∥(m=1)
300
200
100
0
50
100
X
LHR

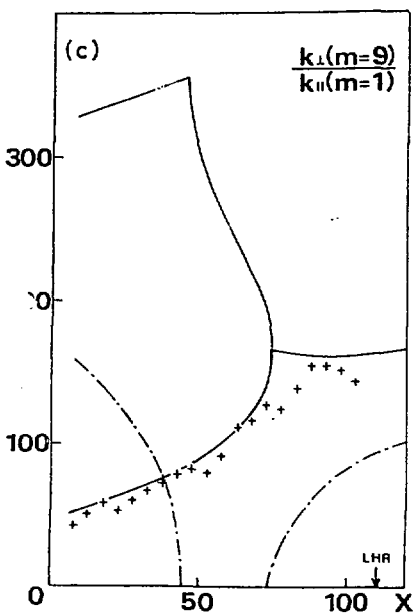
(c)
k⊥(m=9)
k∥(m=1)
300
100
0
50
100
X
LHR

Fig. 4

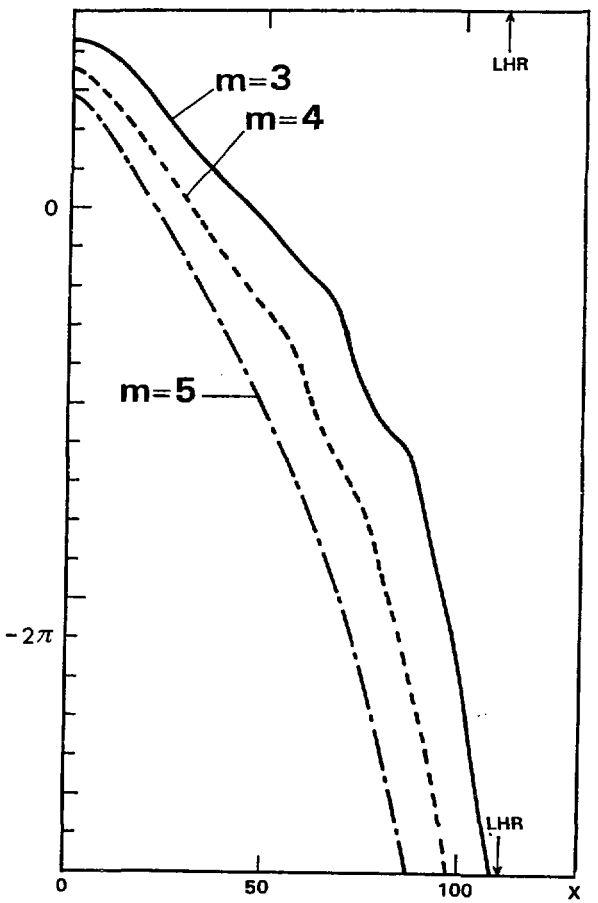

Fig. 5

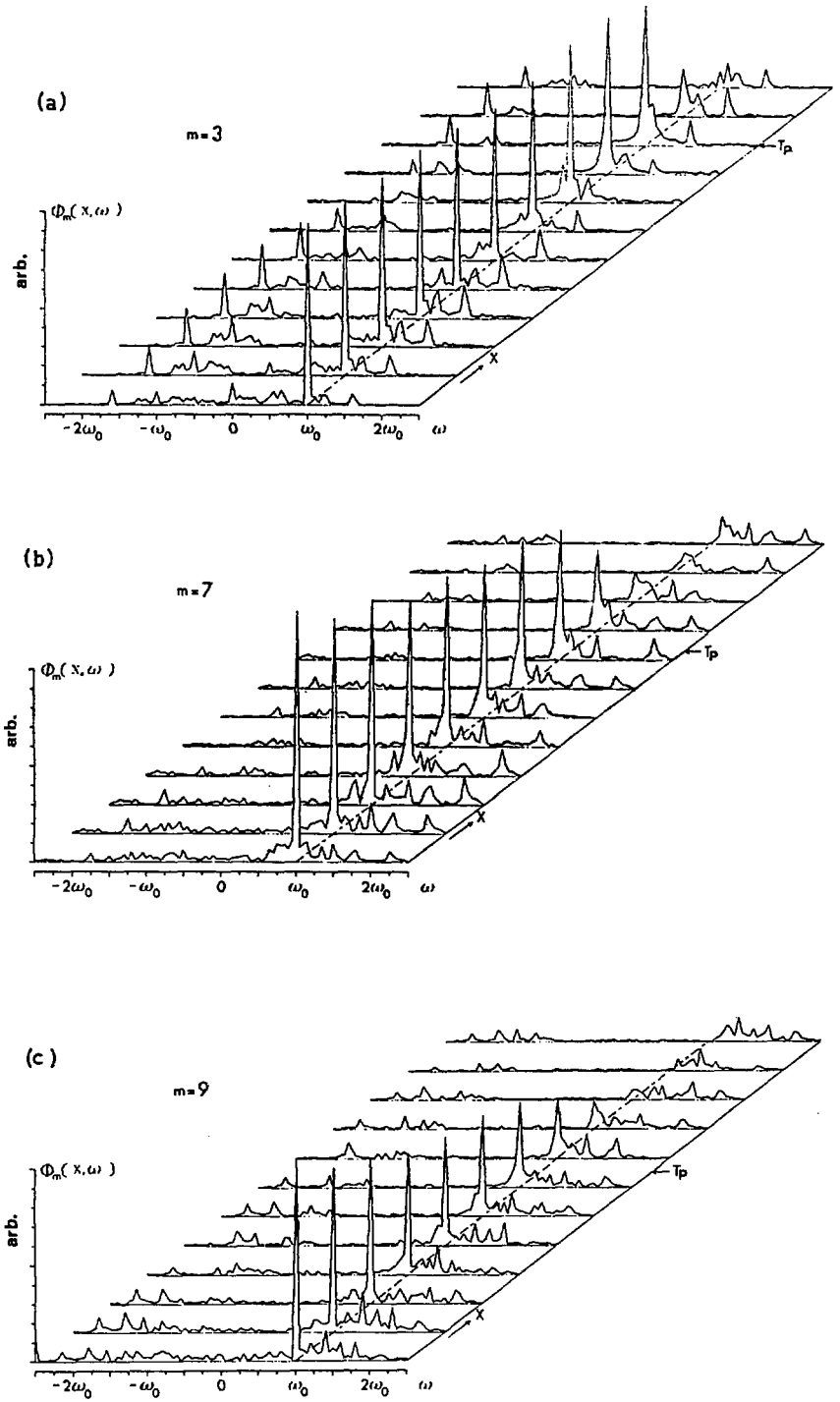
(a)
m=3
$\Phi_m(x,\omega)$
arb.
T_p
x
$-2\omega_0$
$-\omega_0$
0
ω_0
$2\omega_0$
ω
(b)
m=7
$\Phi_m(x,\omega)$
arb.
T_p
x
$-2\omega_0$
$-\omega_0$
0
ω_0
$2\omega_0$
ω
(c)
m=9
$\Phi_m(x,\omega)$
arb.
T_p
x
$-2\omega_0$
$-\omega_0$
0
ω_0
$2\omega_0$
ω

Fig. 6

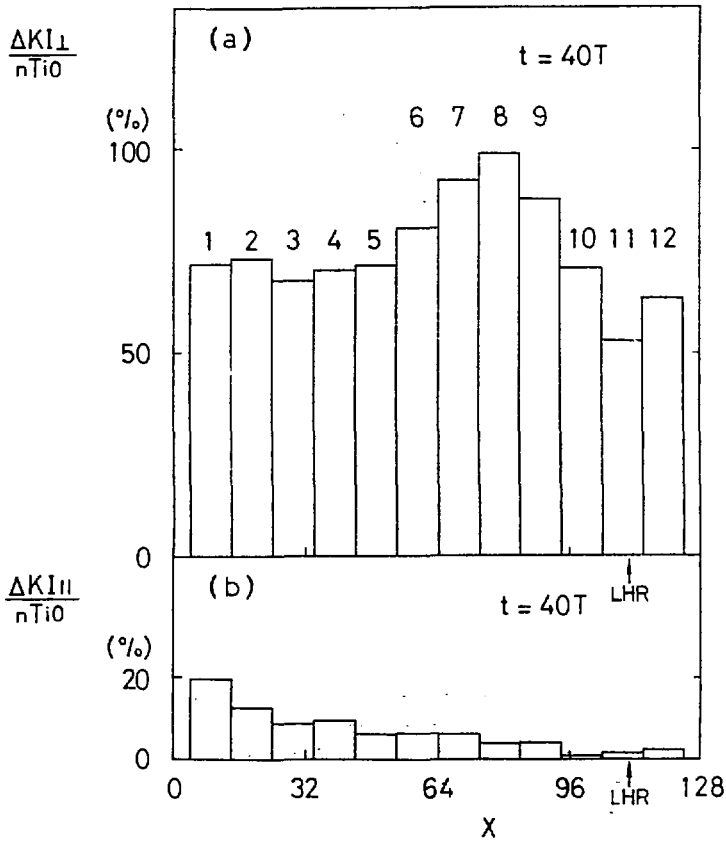
ΔKI⊥ / nTi0
(a)
t = 40T
(%)
100
50
0
1 2 3 4 5 6 7 8 9 10 11 12
ΔKI∥ / nTi0
(b)
t = 40T
LHR
(%)
20
0
0 32 64 96 LHR 128
X

Fig. 7

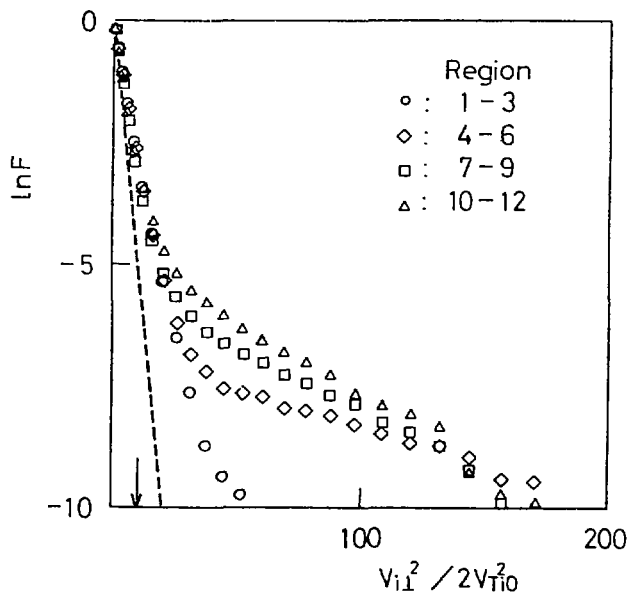
lnF
0
-5
-10
Region
○ : 1 - 3
◇ : 4 - 6
□ : 7 - 9
△ : 10 - 12
100
200
$V_{i\perp}^2 / 2V_{Ti0}^2$

Fig. 8

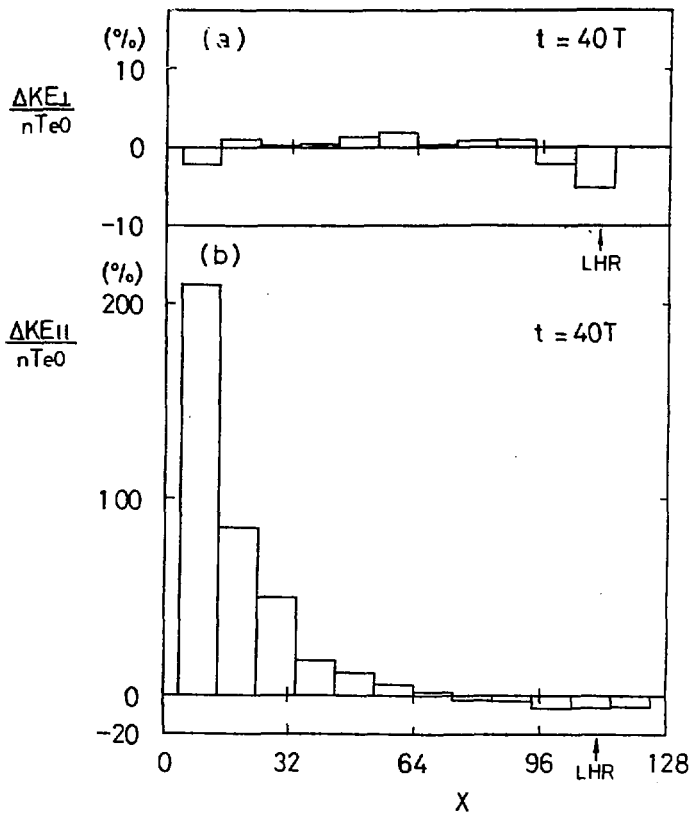
(%)
(a)
t = 40T
10
ΔKE⊥ / nTe0
0
-10
LHR
(%)
(b)
200
ΔKE∥ / nTe0
t = 40T
100
0
-20
0
32
64
96
LHR
128
X

Fig. 9

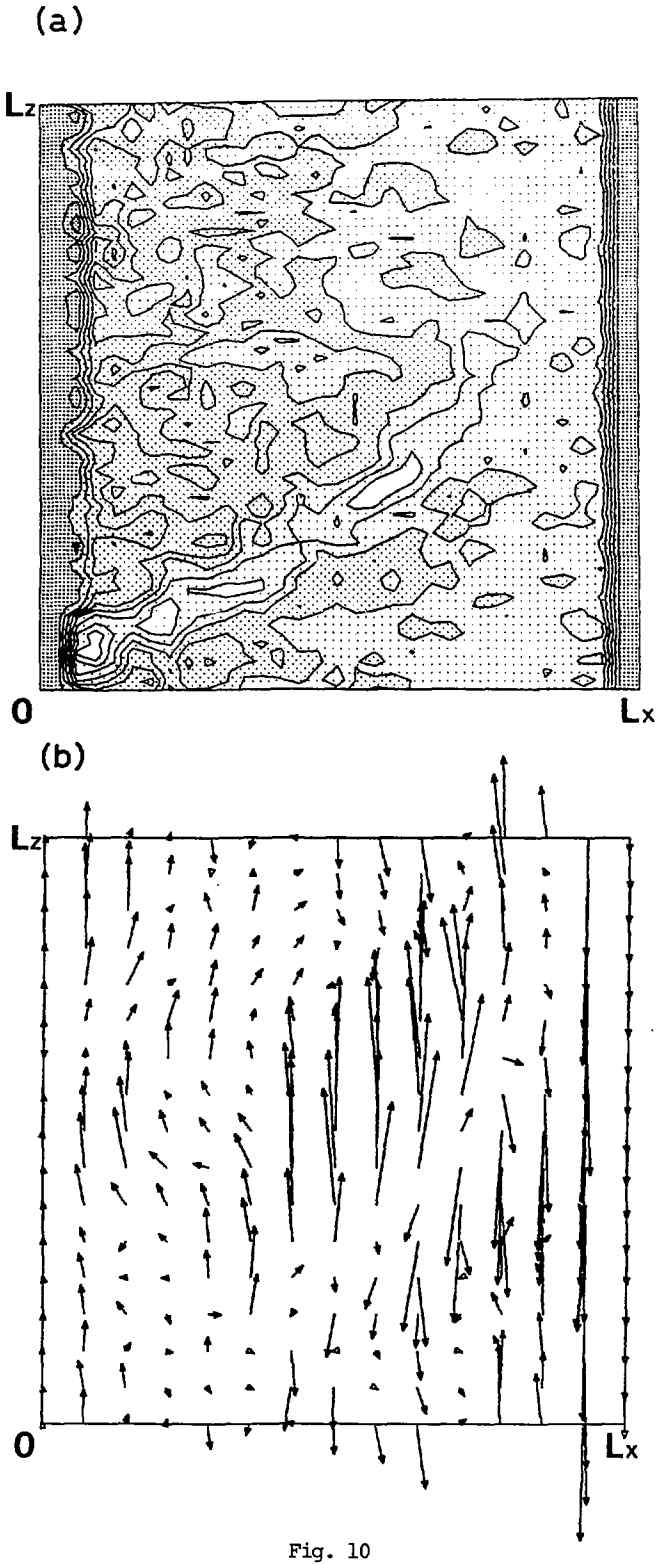

Fig. 10

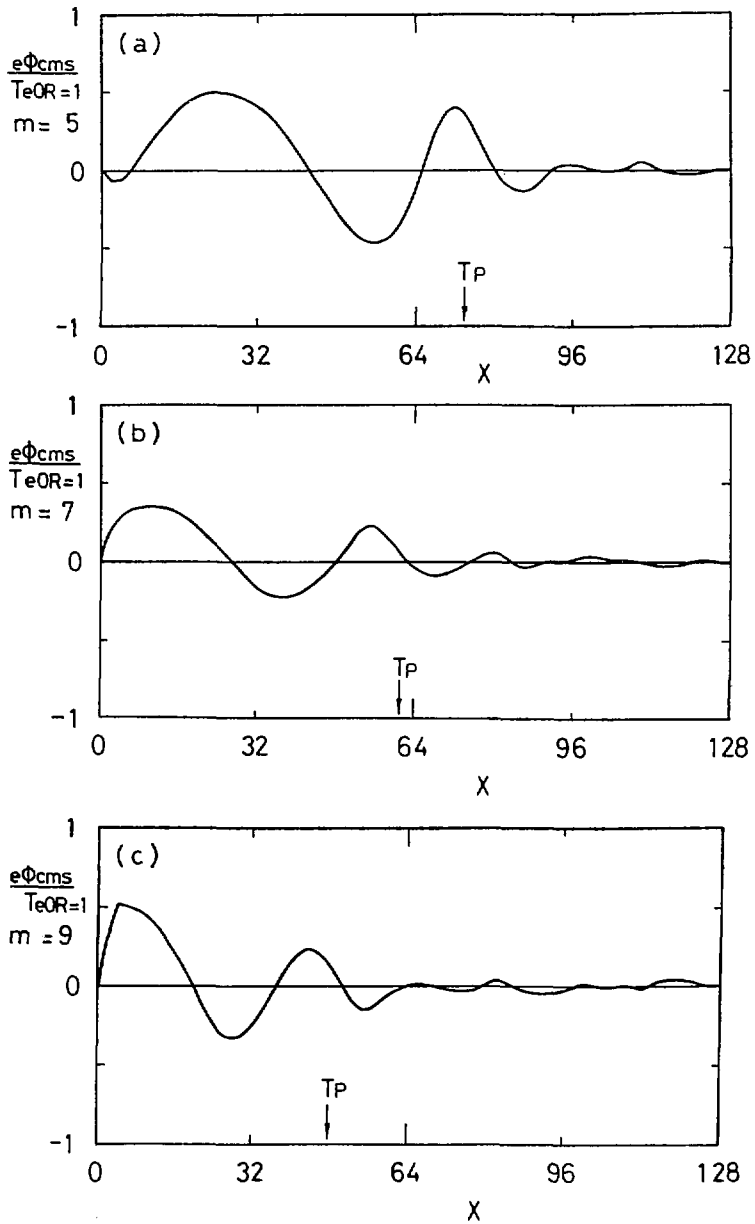
(a)
eΦcms / TeOR=1
m= 5
1
0
-1
Tp
0
32
64
96
128
X
(b)
eΦcms / TeOR=1
m = 7
1
0
-1
Tp
0
32
64
96
128
X
(c)
eΦcms / TeOR=1
m = 9
1
0
-1
Tp
0
32
64
96
128
X

Fig. 11

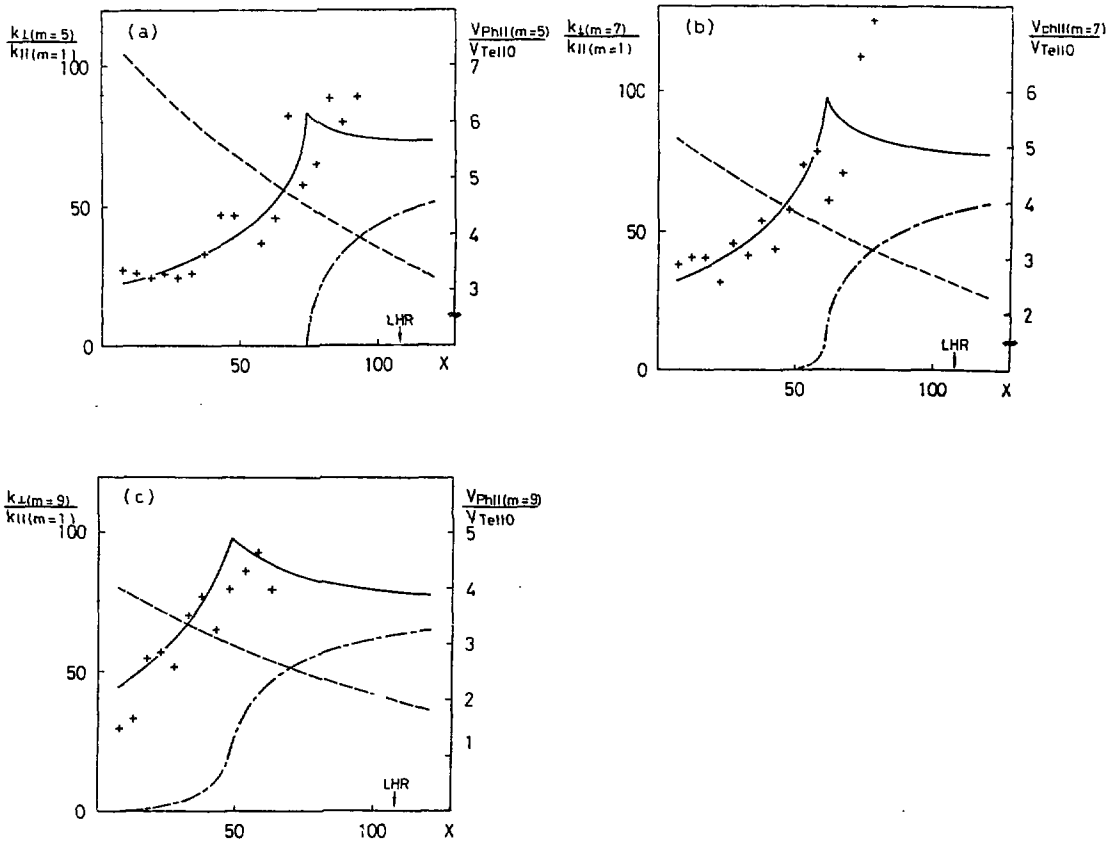
(a)
$k_{\perp(m=5)}/k_{\parallel(m=1)}$
$V_{Phi(m=5)}/V_{Te0}$
100
50
0
50
100
X
LHR
7
6
5
4
3
(b)
$k_{\perp(m=7)}/k_{\parallel(m=1)}$
$V_{Phi(m=7)}/V_{Te0}$
100
50
0
50
100
X
LHR
6
5
4
3
2
(c)
$k_{\perp(m=9)}/k_{\parallel(m=1)}$
$V_{Phi(m=9)}/V_{Te0}$
100
50
0
50
100
X
LHR
5
4
3
2
1

Fig. 12

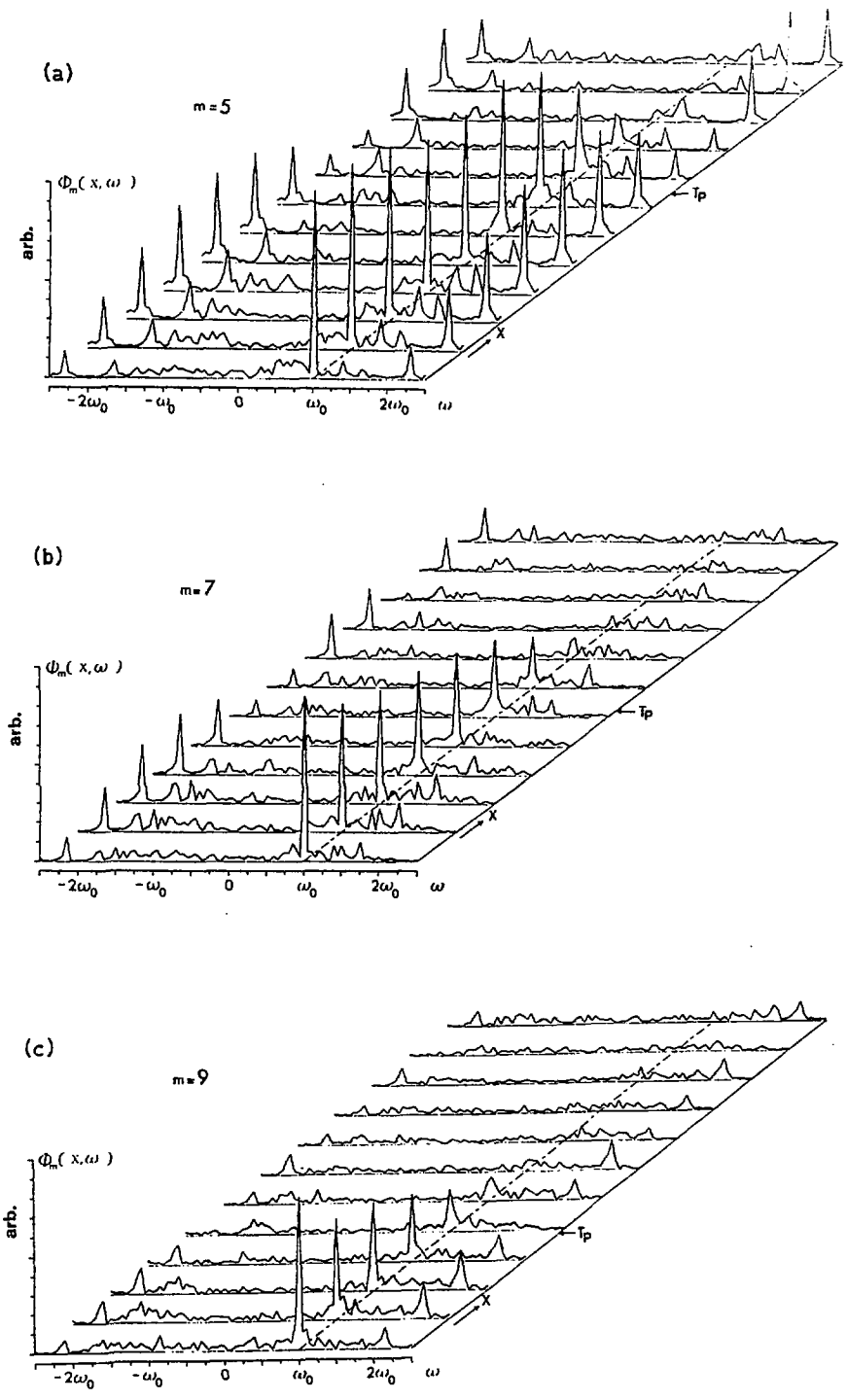
(a)
m=5
$\Phi_m(x,\omega)$
arb.
T_p
x
$-2\omega_0$
$-\omega_0$
0
ω_0
$2\omega_0$
ω
(b)
m=7
$\Phi_m(x,\omega)$
arb.
T_p
x
$-2\omega_0$
$-\omega_0$
0
ω_0
$2\omega_0$
ω
(c)
m=9
$\Phi_m(x,\omega)$
arb.
T_p
x
$-2\omega_0$
$-\omega_0$
0
ω_0
$2\omega_0$
ω

Fig. 13

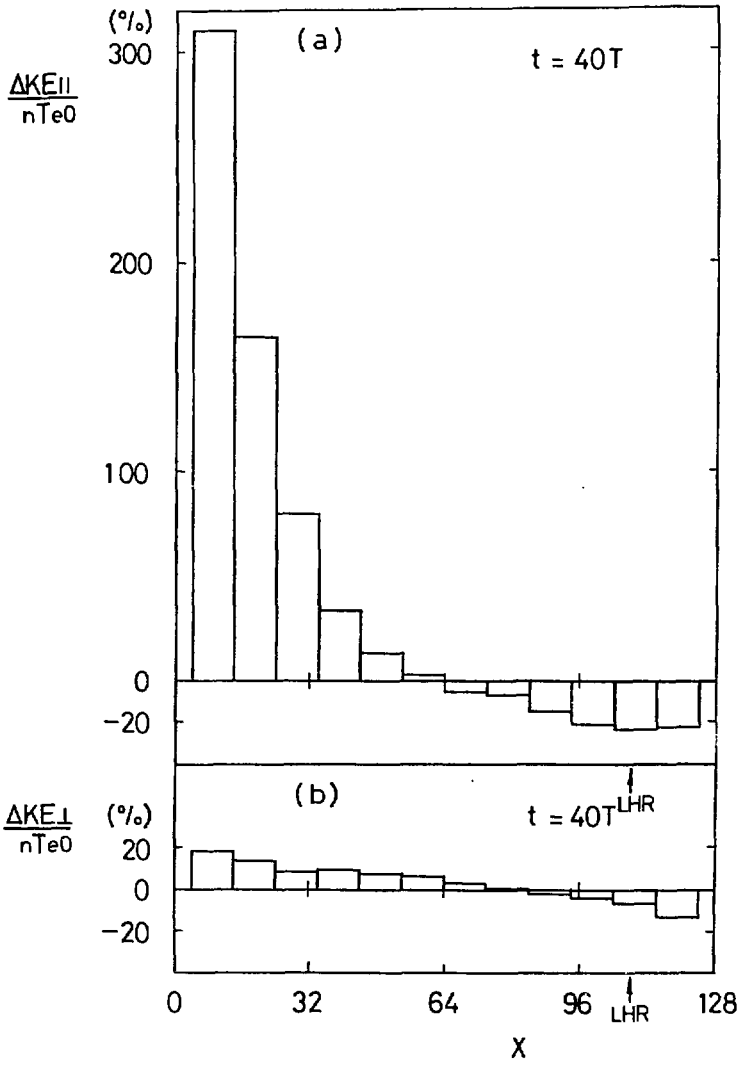
(%)
300
200
100
0
-20
(a)
t = 40T
ΔKE∥ / nTe0
(b)
t = 40T^LHR
ΔKE⊥ / nTe0
(%)
20
0
-20
0
32
64
96
LHR
128
X

Fig. 14

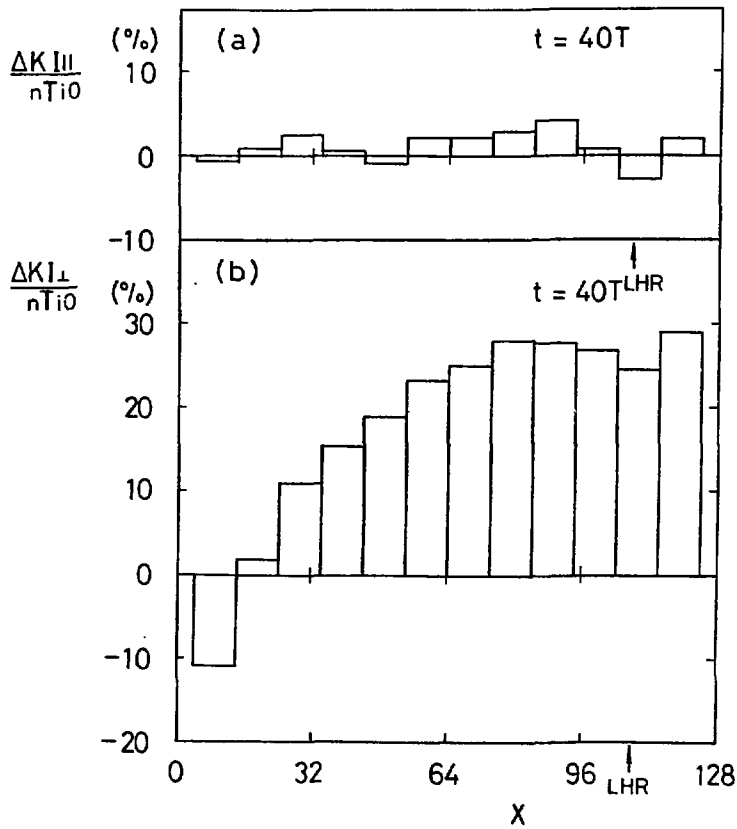
(a)
t = 40T
(%)
10
0
-10
ΔK I∥ / nTi0
(b)
t = 40T LHR
(%)
30
20
10
0
-10
-20
ΔK I⊥ / nTi0
0
32
64
96
LHR
128
X

Fig. 15

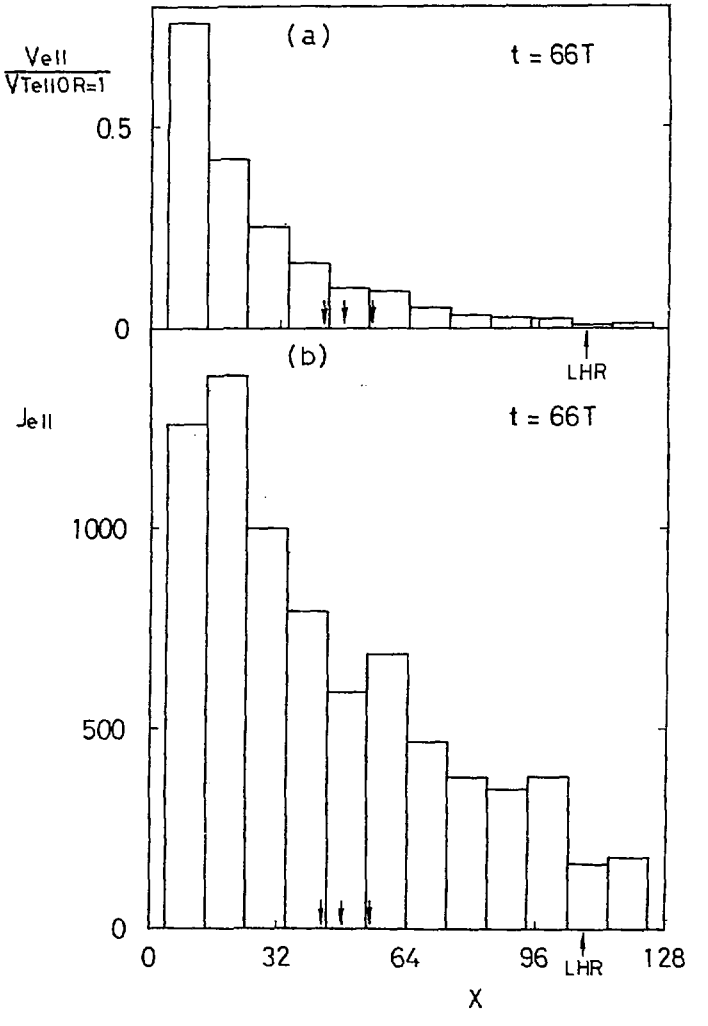
(a)
t = 66T
Vell
VTellOR=1
0.5
0
LHR
(b)
t = 66T
Jell
1000
500
0
0
32
64
96
LHR
128
X

Fig. 16

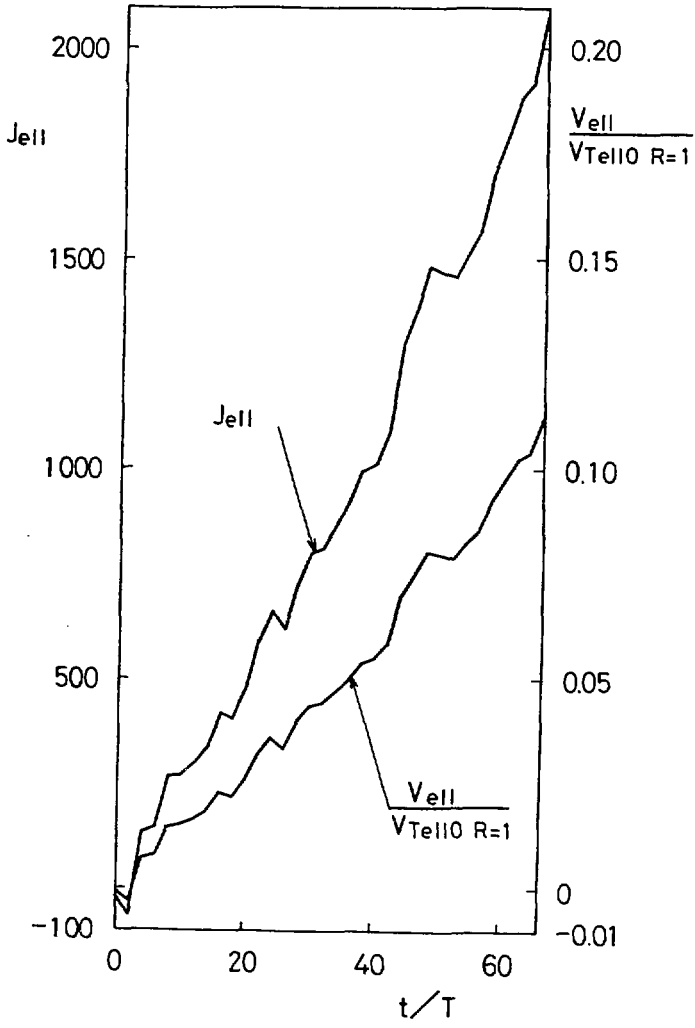
2000
1500
1000
500
-100
Jell
0.20
0.15
0.10
0.05
0
-0.01
Vell / VTell0 R=1
Jell
Vell / VTell0 R=1
0
20
40
60
t/T

Fig. 17

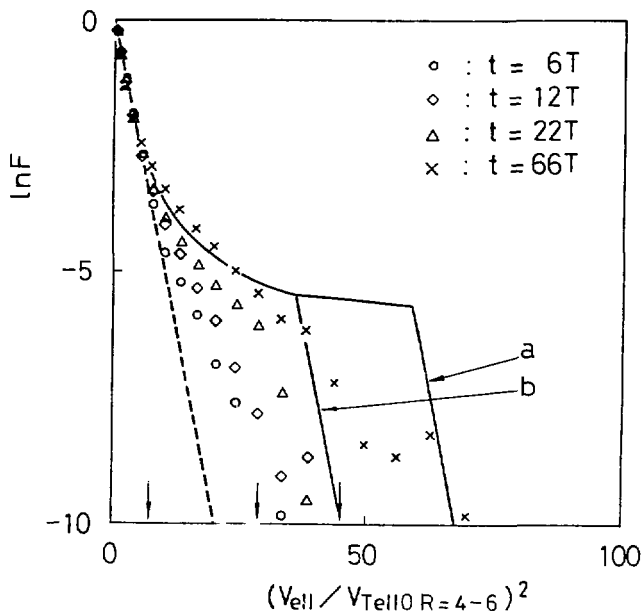

Fig. 18